Geochimica et Cosmochimica Acta 354 (2023) 211–228

Contents lists available at ScienceDirect

Geochimica et Cosmochimica Acta

journal homepage: www.elsevier.com/locate/gca

Activity model for 36 elements in Fe-Ni-Si-S-C liquids with application to terrestrial planet accretion and mantle geochemistry: New data for Ru, Re, Pt, Os, Ti, Nb, and Ta

K. Righter[a,*], A. Boujibar[b], M. Humayun[c], S. Yang[c], R. Rowland II[d,e], K. Pando[e]

[a] NASA JSC, Mailcode XI2, 2101 NASA Pkwy, Houston, TX 77058, USA
[b] Western Washington University, Geology Department ES - 240, Department of Physics and Astronomy, MS 9080, 516, High Street, Bellingham, WA 98225, USA
[c] National High Magnetic Field Laboratory and Department of Earth, Ocean & Atmospheric Science, Florida State University, Tallahassee, FL 32310, USA
[d] Los Alamos National Laboratory, Mail Stop P952, Los Alamos, NM 87545, USA
[e] Jacobs JETS Contract, NASA JSC, Houston, TX 77058, USA

ARTICLE INFO

Associate editor: Hassan Helmy

Keywords:
Siderophile elements
Core formation
Metallic liquid
Trace element

ABSTRACT

Understanding siderophile element partitioning between metal and silicate melts under diverse conditions can be used to place important constraints on the materials and conditions of planetary accretion and core formation, as well as post core formation processes. However, the effects of Si on the partitioning and activity coefficients for these elements are not well known, despite Si likely being one of the dominant light elements in Earth's core. To address this gap in understanding, we have undertaken a systematic study of the highly siderophile elements Re, Pt, Os, and Ru, and the refractory lithophile elements Nb, Ta and Ti at 1600 °C and 1 GPa, to derive epsilon interaction parameters for these elements in FeSi metallic liquids. Positive epsilon interaction parameters were measured for Nb, Ta, Ti, Ru, Re, Pt, and Os, indicating that dissolved Si in Fe liquids causes a decrease in their metal/silicate partition coefficients (or 'silicophobic' behavior). Furthermore, $\varepsilon^{Si}_{Re,Os,\ or\ Ru} > \varepsilon^{S}_{Re,Os,\ or\ Ru}$ which means Si causes a larger decrease in D(metal/silicate) than S, and the chalcophile behavior expected from some elements will be completely masked by the presence of Si in a metallic liquid. The new parameters are used to update an activity model that now includes 36 siderophile elements in Fe-Ni-Si-S-C liquids (27 trace elements considered here). Systematic assessment of these 27 elements shows which have the strongest affinity for Si, C, and S, and also how activity coefficients for these elements would vary during accretion and core formation in Earth, Mars, and Mercury of widely differing fO_2 and core compositional conditions. The activity model is combined with new partitioning expressions for Mo, W, Cr, Re Ru, Pt, and Os and applied to aspects of post core formation mantle geochemistry of Earth, Mars, and Mercury. Our updated expressions show that the BSE Mo/W ratio can easily be achieved with metal/silicate partitioning during growth of the Earth, whereas Re, Os and Ru become lower than and highly fractionated compared with BSE values during core formation and accretion, and thus nearly 99% of their BSE abundances are likely contributed by late accretion. Ru isotopes should be a very good indicator of the source material for the late accretion. The high Pt/Os and Re/Os developed in a deepening magma ocean during the growth of the Earth, indicates ^{186}Os and ^{187}Os isotopes could be coupled if this ancient material remained isolated and subsequently became entrained in mantle plumes and measured in surficial lavas. The extent to which this occurred will be limited by the low Os content of this ancient material, thus requiring mixing as a major component in plume sources. Martian mantle Hf/W ratio stays low during accretion and core formation modelling, suggesting that W isotope anomalies are more likely due to solid/liquid silicate fractionation than to core formation. Finally, Ti contents measured by MESSENGER at Mercury's surface can be explained by segregation of either a metallic core (IW-6 to -8) or metallic core + sulfide (IW-4 to -7.5) followed by mantle melting.

---

* Corresponding author.
E-mail address: kevin.righter-1@nasa.gov (K. Righter).

https://doi.org/10.1016/j.gca.2023.06.014
Received 11 February 2023; Accepted 12 June 2023

1. Introduction

The partitioning of siderophile elements between metallic cores and silicate mantles is sensitive to temperature, pressure, oxygen fugacity, and metallic and silicate liquid composition. Therefore, they can provide key constraints on these conditions during accretion and differentiation of planets and formation of their metallic cores. The non-metal, or light element (e.g., S, C, O, or Si), content of the metallic liquid has a strong influence on D(metal/silicate) [the partition coefficient of an element M between metal and silicate, defined as the concentration (M) in metal / concentration (M) in silicate]. Understanding the relative importance of composition and the intensive parameters P, T, and fO_2 is critical in application of the partitioning data to planetary core formation. Earth's core is known to have a density deficit compared to pure Fe metal; this deficit is commonly attributed to the presence of ~10% of a light element or elements which could be S, C, Si, O, P, and perhaps H (e.g., Hirose et al., 2013, 2021). Silicon is frequently proposed as one of the most abundant light elements in the core (C and S are thought to be relatively minor), based on a wide range of cosmochemical and isotopic evidence (Georg et al., 2007; Armytage et al. 2012; Ziegler et al., 2010), high pressure phase equilibria experiments (Tsuno et al., 2013; Asanuma et al., 2010; Siebert et al., 2013) and deep Earth structure and mineral physics (Mao et al., 2012; Lin et al., 2003; Badro et al., 2007; Sanloup et al., 2004). The effects of dissolved S and C in Fe liquids is well known from extensive studies of moderately siderophile elements (e.g., Chabot et al., 2005; Wood et al., 2014; Jana and Walker, 1997), and highly siderophile elements (e.g., Laurenz et al., 2016; Bennett et al., 2016; Rubie et al., 2016; Righter, 2015), but the effect of Si dissolved in Fe liquid has received less attention, and remains poorly understood for several elements. In addition, Si is the main alloying element with Fe in Mercury's core and the effect of Si content on element partitioning is central to an understanding of Mercury's differentiation.

We have been systematically studying the effects of Si on metal-silicate partitioning for a wide range of siderophile elements such as Mo (Righter et al., 2016), Ge, In, As, Sb (Righter et al., 2017), Au, Pd, Pt, Ga, V, Mn, Cr, Cu (Righter et al., 2018), and Bi, Sn, Cd, Zn (Righter et al., 2019). Combined with additional studies by Tuff et al. (2011), Vogel et al. (2018), and Steenstra et al. (2020) on these and other siderophile elements, our understanding has improved substantially. To more fully understand the effects of Si and explore unknown behavior in several important remaining siderophile elements, we report new experiments designed to quantify the effect of Si on the partitioning of Re, Pt, Os, Ru, Ti, Ta and Nb between metal and silicate melts. These new experiments bring the total number of trace elements well studied in the Fe-Si system to 27, and allow more comprehensive modelling for Fe-Ni-Si-S-C liquids. These new results are used to update the activity model and applied to Earth (for which we have mantle samples provided by peridotite xenoliths and massifs (e.g., Palme and O'Neill, 2014)), Mars (whose geochemistry is constrained by martian meteorites and robotic missions), and Mercury (constrained by MESSENGER data). These examples illustrate the utility of the multi-element activity model for comparative cosmochemistry.

2. Experimental

Experiments at pressure and temperature conditions of 1 GPa and 1600 °C were completed at NASA-JSC using a non-end-loaded piston cylinder apparatus. Pressure was generated using a hydraulic ram and transmitted to the samples through a $BaCO_3$ pressure medium. High temperatures were achieved using graphite furnaces, with temperature monitored using a Type C W-Re thermocouple. Temperature and pressure were calibrated using the detailed approaches described in Righter et al. (2017). Starting compositions were mixtures of ~30% (by mass) metal and ~70% silicate, with these proportions generally producing large analyzable volumes of metal and silicate in the run products. Three different Fe-HSE metal compositions were created by mixing ultra-pure Fe (99.9999%) and different HSE: metallic Fe + 5% Re, metallic Fe + 5% Ru, and metallic Fe + 5% each of Re, Pt, and Os. A range of Fe-HSE-Si metal compositions was created by mixing and homogenizing variable amount of Si metal with the three Fe-HSE metal mixtures (0 to 10 wt% Si). These three compositional series allowed the effects of Si to be explored in a series with a single element (Re or Ru) as well as combination of elements (Re, Pt, Os) with the latter designed to examine implications of Si for the Re-Os and Pt-Os isotopic systems. Silicate composition used was Knippa basalt (given by Lewis et al., 1993) use of which produces MgO-rich melts approaching the composition of those expected in the early Earth (see Section 3), and also for ease of comparison of our results with previous studies that utilized this same composition (Righter et al., 2017, 2018, 2019). The 30% (by mass) metal – 70% silicate mixtures were then loaded into magnorite (partially fused MgO) capsules, pressurized, and then heated to run conditions of 1600 °C.

Guided by our previous work on siderophile elements, experimental runs were of 90 min duration at 1600 °C, allowing sufficient time for an approach to equilibrium (Righter et al., 2010, 2011, 2017, 2018). We have done time series in these 4 previous studies including elements that are 1+ (Cu), 2+ (Co, Ni, Ge, Cd, Zn, Mn), 3+ (In, Ga, Bi, As, Sb, V, Cr), 4+ (Mo, W, Sn), and 5+ (P). These time series have shown that all elements are equilibrated after 90 min at 1600 °C, and so experiments have all been done with this duration. The elements Mo, W, and P (and Nb and Ta) are the highest valence and exhibit the lowest diffusion coefficients of all of these elements (Szumila et al., 2019). Re exhibits diffusion coefficients similar to Mn, among the highest diffusion coefficients (MacKenzie and Canil, 2008; Zhang et al., 2010). The current study includes Re, Pt, Os, Ru, Nb, and Ta. Because Re has similar diffusion coefficients to Mn, and Nb and Ta have comparable kinetics to Mo, W, and P (Szumila et al., 2019), and Pt and Os are 2+ and 3+ respectively and also fall within the range of valence and ionic sizes utilized in our previous experiments, we are confident that these experimental durations are ample for equilibrium for the elements in this study as well. In addition, the silicate liquids in our experiments are more picritic to komatiitic – diffusion is known to be faster in such basic liquids compared to basalt. Diffusion rates for the elements in our study are likely higher than those for the haplobasaltic melts studied by Szumila et al. (2019), thus requiring even shorter times than the previous studies cited above.

3. Analytical

Experimental metals and silicates were analyzed using a combination of electron microprobe analysis (EMPA) at NASA-JSC (Cameca SX100 and JEOL 8530 FEG microprobes), and laser ablation inductively coupled plasma mass spectrometry (LA-ICP-MS) at Florida State University Plasma Analytical Facility of the National High Magnetic Field Laboratory.

EMPA analysis was used for major and minor elements in metals (Fe, Si, P, Re, Pt, Os, Ru, and S) and major and minor elements in silicates (Si, Ti, Al, Fe, Mn, Mg, Ca, Na, K, P, and S) utilizing a variety of mineral and glass standards (Fe, Si, GaP, FeS and other metals; diopside, basaltic glass, potassium feldspar, rutile, rhodonite, Marjalahti pallasite olivine, and albite). Operating conditions included 15 kV accelerating voltage, 30 nA current for metals (20 nA for silicates), and point mode. For both the metals and glasses with coarser grain-size quench texture, a defocused 20–30 μm beam was used for analysis, and typically 30 to 40 points were analyzed and averaged to obtain a representative composition of the metallic and silicate melts. Traverses in both the quenched metallic and silicate liquids reveal a homogeneous pre-quench composition, with no compositional gradients or variation (Supplementary Material, Part 1; Fig. S1). Details of EMPA analysis of HSE in the metal are presented in the Supplementary Material Part 1 (Fig. S2A,B). Analyses are reported in Tables 1–3 and typically have 2σ error (a combination of counting statistics, standards utilized, and matrix corrections)

Table 1
Re series results.

	Re0	Re2	Re4	Re6	Re10
Silicate					
SiO_2 (wt%)	31.3(1.6)	33.3(1.7)	43.2(2.2)	42.8(2.1)	42.4(2.1)
TiO_2	3.69(7)	3.83(8)	3.42(7)	3.24(6)	1.94(4)
Al_2O_3	11.5(2)	12.6(3)	11.5(2)	11.7(2)	10.6(2)
FeO	11.85(12)	5.21(5)	0.47(1)	0.12(1)	0.010(1)
MnO	0.15(1)	0.16(1)	0.15(1)	0.10(1)	0.030(2)
MgO	23.4(5)	28.7(6)	24.9(5)	25.0(5)	32.3(6)
CaO	13.37(13)	12.84(13)	12.31(12)	12.70(9)	10.51(11)
Na_2O	3.5(2)	3.3(2)	3.3(2)	3.2(2)	2.7(1)
K_2O	1.95(2)	1.92(2)	1.92(2)	1.86(2)	1.70(2)
P_2O_5	0.91(2)	0.28(1)	0.030(2)	0.030(2)	0.030(3)
Total	101.60	102.10	101.20	100.70	102.30
Cu (ppm)	6.7(7)	3.4(3)	1.8(2)	1.4(1)	0.97(10)
Ga	11.6(1.2)	5.2(5)	2.2(2)	1.9(2)	2.1(2)
Zn	68.3(6.8)	60.3(6.0)	13.9(1.4)	9.2(9)	3.0(3)
V	180(18)	200(20)	57.2(5.7)	9.7(9)	0.98(10)
Cr	130(13)	209(21)	87(9)	23(2)	3.0(3)
Ni	1.7(2)	1.3(1)	1.8(2)	1.0(1)	1.0(1)
Co	0.40(4)	0.23(2)	0.21(2)	0.17(2)	0.31(3)
Pb	4.3(4)	1.1(1)	0.22(2)	0.094(9)	0.082(8)
As	0.34(3)	0.33(3)	0.28(3)	0.25(3)	0.28(3)
Nb	70.1(7.0)	73.6(7.4)	27.3(2.7)	1.2(1)	0.043(4)
Ta	4.3(4)	4.4(4)	3.7(4)	2.2(2)	0.075(8)
Sn	0.30(3)	0.089(9)	0.057(6)	0.039(4)	0.028(3)
Re	**0.11(2)**	**0.11(2)**	**0.049(10)**	**0.054(10)**	**0.73(14)**
Metal					
Si (wt%)	n.d.	0.0060(1)	0.75(1)	5.89(6)	16.3(2)
Fe	93.72(94)	94.47(94)	94.11(94)	88.61(89)	78.7(8)
P	0.054(1)	0.54(1)	0.71(1)	0.59(1)	0.6(1)
Re	**5.53(11)**	**4.2(1)**	**3.84(8)**	**3.73(7)**	**3.13(6)**
Cu (ppm)	308(31)	363(36)	256(26)	170(17)	165(17)
Ga	33(3)	42(4)	44(4)	41(4)	42(4)
Zn	20(2)	36(4)	84(8)	83(8)	84(8)
V	2.0(2)	16(2)	264(26)	363(36)	341(34)
Cr	13(1)	100(10)	534(53)	605(61)	626(63)
Ni	745(75)	591(59)	543(54)	477(48)	446(45)
Co	174(17)	138(14)	123(13)	114(11)	107(11)
Pb	3.5(4)	27.1(2.7)	24.6(2.5)	16.7(1.7)	28.2(2.8)
Total	99.31	99.22	99.41	98.82	98.70
X_{FeO}	0.093	0.039	0.0036	0.0009	0.0001
X_{Fe}	0.77	0.81	0.81	0.74	0.62
X_{Si}	0.000	0.000	0.013	0.098	0.25
ln (1-X_{Si})	0	−0.0001	−0.0129	−0.103	−0.293
ΔIW	−1.84(4)	−2.63(5)	−4.70(15)	−5.80(20)	−7.84(33)
ln K_d (Fe-Re)-ln (γFe)	8.83	6.87	2.83	0.204	−7.22
ln K_d (Fe-Cu)+ 0.5ln(γFe)	2.51	2.95	2.02	1.15	0.250
ln K_d (Fe-Ga)-0.5ln(γFe)	−2.28	−2.50	−5.13	−6.97	−10.5
ln K_d (Fe-Zn)	−3.55	−3.67	−3.75	−4.66	−5.89
ln K_d (Fe-V)-0.5ln(γFe)	−7.82	−7.11	−6.62	−6.43	−7.71
ln K_d (Fe-Cr)-0.5ln(γFe)	−9.96	−9.67	−10.7	−11.0	−12.7
ln K_d (Fe-Ni)	3.76	2.97	0.136	−0.689	−3.12
ln K_d (Fe-Co)	3.76	3.25	0.8821	−0.348	−3.38
ln K_d (Fe-Pb)	0.252	0.0233	−0.835	−1.68	−3.38
lnK_d (Fe-P)-1.5ln (γFe)	−10.703	−11.333	−20.368	−26.488	−37.809

Table 2
Ru series results.

	Ru0	Ru2	Ru4	Ru6	Ru10
Silicate					
SiO_2 (wt%)	30.7(1.7)	31.5(1.6)	38.2(1.9)	36.5(1.8)	36.7(1.8)
TiO_2	3.58(7)	3.73(7)	2.16(4)	3.09(6)	1.62(3)
Al_2O_3	10.0(2)	10.2(2)	6.1(1)	9.6(2)	10.2(2)
FeO	11.58(12)	9.72(10)	0.17(1)	0.040(4)	0.010(2)
MnO	0.15(1)	0.16(1)	0.090(2)	0.058(2)	0.012(1)
MgO	24.7(5)	24.4(5)	42.1(8)	34.5(7)	32.8(7)
CaO	12.80(13)	13.10(13)	7.70(8)	11.20(11)	12.50(13)
Na_2O	3.6(2)	4.0(2)	2.2(1)	3.11(2)	3.8(2)
K_2O	1.92(2)	2.20(2)	1.29(1)	1.91(2)	2.21(2)
P_2O_5	0.97(2)	0.92(2)	0.0040(4)	0.0020(2)	0.0030(3)
Total	99.90	99.96	99.98	100.01	99.90
V (ppm)	180(18)	181(18)	38(4)	7.0(7)	1.0(1)
Cr	141(14)	155(16)	39(4)	10(1)	3.0(3)
Nb	66(7)	72(7)	16.7(1.7)	1.1(1)	0.040(4)
Ta	3.8(4)	4.0(4)	2.7(3)	1.8(2)	0.10(1)
Ru	**0.030(6)**	**0.054(9)**	**0.054(9)**	**0.099(20)**	**0.052(9)**
Metal					
Si (wt%)	0.41(1)	0.18(1)	0.87(2)	4.63	13.8645
Fe	92.56(93)	92.83(92)	92.83(92)	87.38	80.07
P	0.024(1)	0.29(1)	0.77(2)	0.8893	0.9702
Ru	**6.88(14)**	**6.53(13)**	**5.23(10)**	**6.68(13)**	**3.67(7)**
V (ppm)	3.0(3)	4.0(4)	396(40)	493(49)	394(40)
Cr	16(2)	21(2)	585(59)	601(60)	589(59)
Nb	0.27(3)	0.060(6)	30(3)	97(10)	36(4)
Ta	0.050(5)	0.010(1)	0.12(1)	2.9(3)	1.6(2)
Ti	124(12)	41(4)	112(11)	810(81)	10300(1000)
Total	99.88	99.83	99.70	99.58	98.58
X_{FeO}	0.093	0.078	0.0012	0.0003	0.0001
X_{Fe}	0.95	0.95	0.94	0.86	0.71
X_{Si}	0.008	0.004	0.018	0.091	0.245
ln (1-X_{Si})	−0.00850	−0.0037	−0.0177	−0.0949	−0.282
ΔIW	−2.02(4)	−2.18(4)	−5.78(18)	−6.92(22)	−7.95(41)
ln K_d (Fe-Ru)-ln (γFe)	9.53	8.59	0.123	−2.82	−5.19
ln K_d (Fe-V)-0.5ln(γFe)	−8.26	−7.99	−8.10	−8.13	−8.47
ln K_d (Fe-Cr)-0.5ln(γFe)	−10.5	−10.6	−12.1	−12.7	−13.2
ln K_d (Fe-Nb)-1.5ln(γFe)	−6.22	−6.58	−16.9	−20.1	−23.1
ln K_d (Fe-Ta)-1.5ln(γFe)	−6.22	−6.58	−16.9	−20.1	−23.1
ln K_d (Fe-Ti)-0.5ln(γFe)	−10.3	−11.7	−18.4	−19.4	−18.6
ln K_d (Fe-P)-1.5ln(γFe)	−20.6	−16.2	−29.0	−34.3	−40.2

~2% for most elements and ~5% for Si, Al, Mg, and Na.

Re, Pt, Os, Ru, Ta, Ti, and Nb are all present at low concentrations in the silicates and glasses (typically < 100 ppm), could not be measured using EMPA, and instead were measured by LA-ICP-MS using Electro-Scientific Instruments (ESI) New Wave UP193FX excimer (193 nm) laser ablation system coupled to a Thermo Element XR Inductively Coupled Plasma Mass Spectrometer (ICP-MS). Laser fluence was 2 GW/cm^2. Masses measured were: ^{29}Si, ^{31}P, ^{47}Ti, ^{51}V, ^{53}Cr, ^{55}Mn, ^{57}Fe, ^{59}Co, ^{60}Ni, ^{63}Cu, ^{66}Zn, ^{71}Ga, ^{93}Nb, ^{102}Ru, ^{103}Rh, $^{105+106}$Pd, ^{181}Ta, ^{182}W, ^{185}Re, ^{192}Os, ^{193}Ir, ^{195}Pt, ^{197}Au, ^{208}Pb, and other elements as described by Yang et al. (2015; 2018). For silicates ^{29}Si was used for internal normalization while for metal + sulfide, ^{57}Fe was used for internal normalization. The relevant isobaric interferences are discussed in Yang et al. (2018). NIST SRM 610 glass and USGS basaltic glasses BHVO-2G, BIR-1G, and BCR-2G were used to determine relative sensitivity factors (RSF) for lithophile elements (Jochum et al., 2011), while group IVB iron meteorite Hoba (Walker et al., 2008), NIST SRM 1263a (Campbell et al., 2002) and group IIA iron meteorite Filomena (Wasson et al., 1989) were used to determine RSFs for siderophile elements (Humayun et al., 2007; Gaboardi and Humayun, 2009; Humayun, 2012). Comparison of standards analyzed as unknowns to published values are given in Supplementary Material, Part 2 (Table S2). The metal portions of the samples were typically measured using a 20 μm raster at 5 μm/s and 20 Hz,

Table 3

Re-Pt-Os series results.

	RePtOs-003	**RePtOs-007**	**RePtOs-009**	**RePtOs-013**	**RePtOs-014**	**RePtOs-015**	**RePtOs-016**
Silicate							
SiO_2 (wt%)	32.0(1.6)	34.7(1.7)	40.0(2.0)	38.7(1.9)	36.5(1.8)	29.5(1.5)	36.4(1.8)
TiO_2	2.62(5)	1.99(4)	1.26(3)	2.42(5)	2.22(4)	1.96(4)	2.57(5)
Al_2O_3	12.1(2)	14.6(3)	11.5(2)	12.2(2)	10.5(2)	8.4(2)	12.5(3)
FeO	2.91(3)	0.030(1)	0.010(1)	0.040(1)	0.040(1)	9.75(10)	0.10(1)
MnO	0.15(1)	0.040(1)	0.020(1)	0.080(2)	0.060(2)	0.15(1)	0.10(1)
MgO	33.1(7)	35.8(7)	32.1(6)	31.3(6)	36.6(7)	38.5(8)	32.9(7)
CaO	11.87(12)	9.12(9)	10.21(10)	10.56(11)	9.64(10)	7.55(8)	10.68(11)
Na_2O	3.0(2)	2.1(1)	2.8(2)	2.7(1)	2.6(1)	2.2(1)	2.6(1)
K_2O	2.15(2)	1.56(2)	2.05(2)	2.01(2)	1.84(2)	1.59(2)	1.97(2)
P_2O_5	0.09(1)	0.0015(2)	0.0017(2)	0.0017(2)	0.0015(2)	0.41(2)	0.0010(1)
SO_2	0.010(1)	0.020(2)	0.020(2)	0.020(2)	0.020(2)	0.010(1)	0.017(2)
Total	99.89	100.11	99.78	99.91	99.54	100.10	99.94
Ga (ppm)	8.3(8)	5.2(5)	6.3(6)	5.7(6)	5.4(5)	8.8(9)	6.5(7)
Zn	41.4(4.1)	71(7)	32(3)	20(2)	11(1)	56(6)	11(1)
V	147(15)	2.9(3)	0.86(9)	5.4(5)	5.0(5)	156(16)	12.3(1.2)
Cr	116(12)	6.8(7)	2.1(2)	27(3)	6.8(7)	137(14)	21(2)
Pb	0.86(9)	0.081(9)	0.14(2)	0.23(2)	0.061(6)	1.5(2)	0.11(1)
As	0.33(3)	0.25(3)	0.29(3)	0.28(3)	0.27(3)	0.21(2)	0.32(3)
Nb	45.6(4.6)	0.098(9)	0.030(3)	0.35(4)	0.32(3)	33.0(3)	2.0(2)
Ta	2.4(2)	0.27(3)	0.027(3)	0.64(6)	0.63(6)	1.7(2)	1.7(2)
Sn	0.11(1)	0.20(2)	0.15(2)	0.18(2)	0.063(6)	0.17(2)	0.086(9)
Re	0.18(4)	0.23(5)	1.9(4)	4.0(8)	0.15(3)	0.34(7)	0.27(5)
Pt	0.24(5)	0.56(11)	0.37(7)	0.95(19)	0.59(12)	0.5(1)	0.047(9)
Os	0.18(4)	0.35(7)	0.54(11)	0.31(6)	0.23(5)	0.33(7)	0.013(3)
Metal							
Si (wt%)	0.18(1)	9.56(10)	17.07(17)	7.75(8)	6.40(6)	0.220(2)	3.57(4)
Fe	96.51(96)	84.58(85)	76.71(77)	89.80(90)	91.20(91)	98.10(98)	94.6(9)
P	0.69(1)	0.76(1)	0.75(1)	0.77(1)	0.75(1)	0.27(1)	0.600(6)
S	0.050(1)	0.021(1)	0.019(1)	0.023(1)	0.018(1)	0.068(1)	0.0175(2)
Re	**0.52(1)**	**1.53(3)**	**1.06(2)**	**0.170(3)**	**0.200(4)**	**0.190(4)**	**0.094(2)**
Pt	**1.10(2)**	**1.15(2)**	**1.00(2)**	**0.50(9)**	**0.55(1)**	**0.66(1)**	**0.36(1)**
Os	**0.54(1)**	**1.45(3)**	**0.96(2)**	**0.18(1)**	**0.200(4)**	**0.190(4)**	**0.103(2)**
As (ppm)	5.6(6)	5.0(5)	4.9(5)	5.5(6)	5.6(6)	7.3(7)	5.2(5)
Nb	0.20(2)	88(9)	54(5)	32(3)	27(3)	0.05(1)	12(2)
Ta	0.0030(3)	4.7(5)	2.7(3)	0.76(8)	0.74	0.005(1)	0.17(2)
Sn	6.1(6)	6.1(6)	6.3(6)	6.8(7)	6.8(7)	8.0(8)	6.4(6)
Ga	37(4)	42(4)	33(3)	40(4)	43(4)	35(3)	42(4)
Zn	38(4)	130(13)	39(4)	94(9)	64(7)	18(2)	135(14)
V	30(3)	500(50)	391(39)	393(39)	417(42)	5.8(6)	310(31)
Cr	142(14)	590(60)	522(52)	1500(150)	716(72)	34(3)	603(60)
Pb	38(4)	26(3)	27(3)	38(4)	43(4)	36(4)	33(3)
Total	99.63	99.20	97.69	99.40	99.44	99.71	99.47
X_{FeO}	0.022	0.0002	0.0001	0.0003	0.0003	0.072	0.0008
X_{Fe}	0.8899	0.4844	0.4852	0.6667	0.5363	0.8956	0.8023
X_{Si}	0.003	0.109	0.215	0.114	0.075	0.004	0.060
$\ln(1-X_{Si})$	−0.00337	−0.115	−0.242	−0.121	−0.0778	−0.00404	−0.0621
ΔIW	−3.21(9)	−6.71(28)	−7.32(39)	−6.70(27)	−6.49(26)	−2.19(4)	−6.05(24)
$\ln K_d$ (Fe-Re)-ln(γFe)	2.92	−4.50	−8.24	−9.30	−5.61	3.63	−5.68
$\ln K_d$ (Fe-Os)-ln(γFe)	2.66	−5.47	−6.72	−7.83	−6.96	3.26	−3.88
$\ln K_d$ Pt	7.32	2.18	0.991	1.72	2.14	7.36	5.46
$\ln K_d$ (Fe-Ga)-0.5ln(γFe)	−4.04	−9.84	−11.2	−9.72	−9.45	−2.38	−8.62
$\ln K_d$ Zn	−3.85	−7.64	−8.66	−6.45	−6.19	−3.68	−4.63
$\ln K_d$ (Fe-V)-0.5ln(γFe)	−7.14	−6.80	−6.74	−7.39	−7.10	−7.06	−7.25
$\ln K_d$ (Fe-Cr)-0.5ln(γFe)	−9.68	−11.8	−11.7	−12.0	−11.2	−9.48	−11.4
$\ln K_d$ Pb	0.0282	−2.49	−3.61	−2.89	−1.39	0.624	−1.39
$\ln K_d$ (Fe-As)-0.5ln(γFe)	6.50	0.269	−0.829	0.524	0.729	8.99	1.53
$\ln K_d$ (Fe-Nb)-1.5ln(γFe)	−5.36	−3.28	−4.15	−5.29	−3.75	−3.46	−6.20
$\ln K_d$ (Fe-Ta)-1.5ln(γFe)	−9.56	−6.21	−7.14	−9.04	−8.59	−5.76	−10.5
$\ln K_d$ (Fe-Sn)-ln(γFe)	−5.23	−3.96	−3.46	−6.38	−6.13	−2.03	−7.37
$\ln K_d$ (Fe-P)-1.5ln(γFe)	−13.563	−28.391	−31.463	−28.181	−27.128	−10.148	−24.892

collected with 150 runs. In some experiments the quenched metallic liquids were analyzed using an average of 3 to 4 scan lines across the metallic portion due to the coarser-grained textures (see Section 4.1) and heterogeneity that would result from analysis of smaller regions. Because of the presence of quench olivine and MgO crystals (the latter from reaction with the capsule) scattered throughout the quenched silicate liquids, a 50 µm line was scanned at 10 µm/s, 20 Hz, 100 runs. The linear scans allowed more representative sampling of the coarse-grained silicate portions, and easier interpretation of instances where there was overlap with MgO crystals. Single values from the scan were examined to screen out spikes associated with MgO crystals. The relative standard deviation (RSD) of HSE abundances in metal from each of the runs was ~2%, and RSD of HSE in the silicate portions averaged ~20% (Tables 1–3).

4. Results

4.1. Phase equilibria and equilibrium

Metallic liquid was equilibrated with silicate liquid in all experiments. Metallic and silicate liquids quench to a complex fine-grained multi-phase intergrowth of quench crystals. Both metal and silicate phases must be analyzed with a beam size that is larger than the scale of the intergrowths, and averaged over many points to obtain a representative analysis of the run products. A representative analysis of the metallic liquid is obtained by averaging over many points. For the metals, line scans were carried out in a spoke-like pattern on each large metallic sphere so that the average of the scans captures the representative bulk composition of the quenched metallic phase (e.g., experiment Os-Pt-Re-013; Supplementary Material Part 3). MgO-rich silicate melts (MgO > 20%) are difficult to quench to a glass even with the high quench rates of a piston-cylinder experiment. Our silicate run products typically contain a multi-phase mixture of coarse-grained, skeletal-shaped, quench silicate crystals and glass (Fig. 1 and Supplementary Material, Part 3; Fig. S3). For the silicates, the analyses were carried out as line scans across regions that were free of coarse MgO or olivine grains that were unrepresentative of the liquids. This approach was also described in detail by Righter et al. (2018) for Au, Pd, and Pt analysis.

Many HSE studies have reported nuggets in experiments utilizing pure HSE rods or metals in solubility studies (Ertel et al., 1999; O'Neill et al., 1995). Some of these studies have observed micronuggets that could be seen in BSE images (Cottrell and Walker, 2006), while others

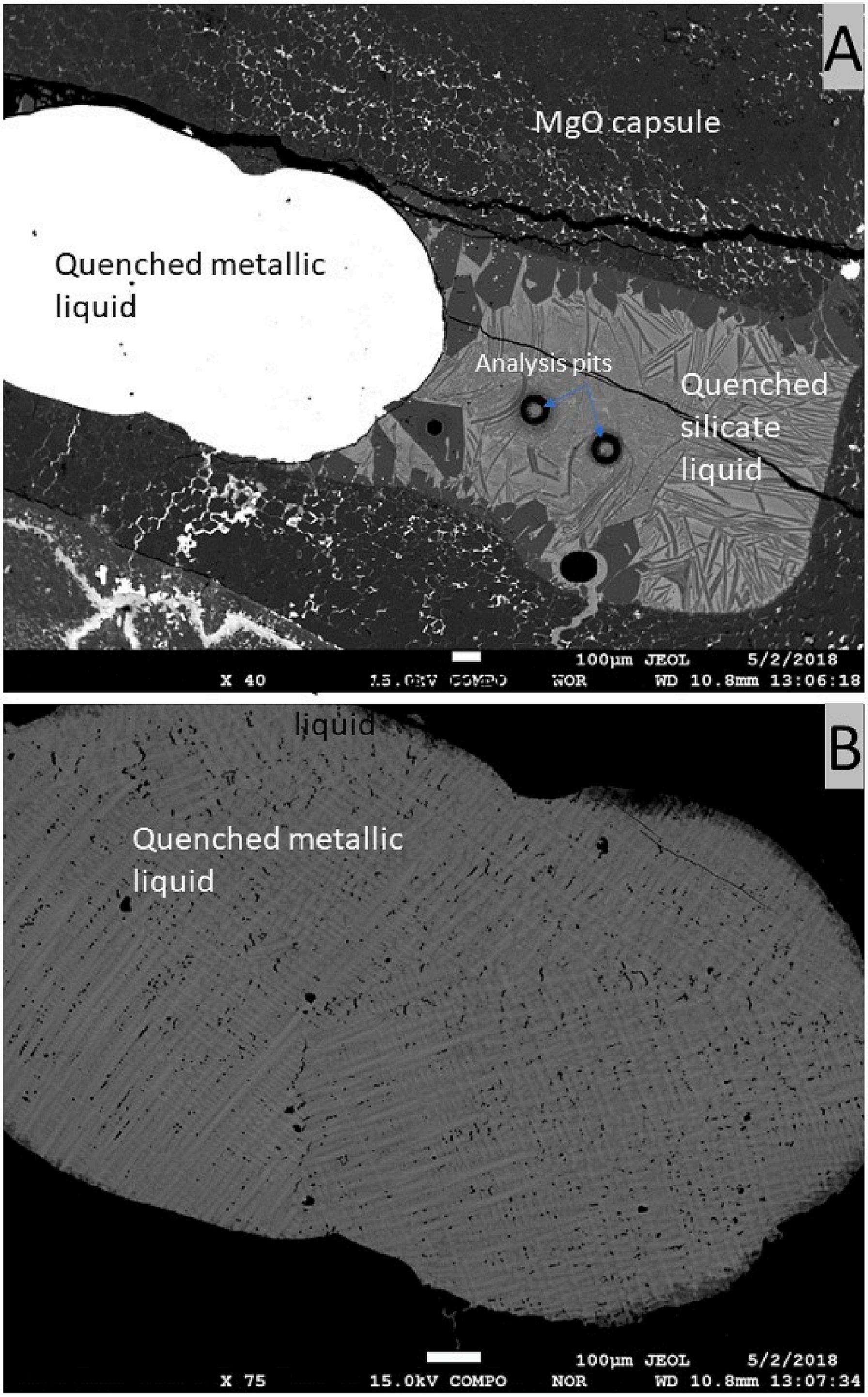

Fig. 1. BSE images of typical experimental run product experiment Re-6B (6% Si added to Fe metal) The top image (A) shows the full sample including the metallic and silicate portions, and the lower image (B) shows the metallic portion at higher magnification and optimal contrast to illustrate the quench textures. The silicate portions quenched to a mixture of glass and quench crystals and the largest areas and finest grained quench textured regions were selected for analysis. Laser spots are shown in Fig. 1A in the silicate portion and illustrate the typical sampling approach. All experiments carried out at 1 GPa and 1600 °C, in MgO capsules, which reacted slightly with the silicate melt.

had a solubility signature of nuggets but no visible evidence (nanonuggets) (Ertel et al., 2008). Use of lower doping levels and/or centrifuging (compared to high levels or pure HSE metal sources) has led to results with nugget-free glasses (e.g., Medard et al., 2015; Righter et al., 2015; Brenan and McDonough, 2009). Measurements in these cases are in better agreement with each other, and could monitor spikes of HSE during analysis with LA-ICP-MS. No HSE micronuggets were observed in our experiments (see also Righter et al., 2018). If a micronugget was present, but not observed in macro-scale or in micro-scale imaging, the presence of HSE particles could be detected by observation of HSE “spikes” (Re, Ru, Pt, Os) during analysis of the silicates. If detected, such spikes could be removed for data reduction of the HSEs, as also explained in Righter et al. (2018). This best effort at avoiding nugget effects does not necessarily eliminate the problem, but it is an improvement; this is an active area of research (Malavergne et al., 2016; Steenstra et al., 2022).

4.2. Oxygen fugacity calculations

The goal of our experiments is to study the effect of dissolved Si in Fe metallic liquids. When Si metal is added to the experimental composition, it creates FeSi metallic liquids with variable Si content, as intended, but the increased Si content also causes a decrease in fO_2. Because fO_2 is an important variable controlling element partitioning between metal and silicate this value must be calculated for each experiment. In metal-silicate studies oxygen fugacity is typically calculated relative to the iron-wüstite (IW) oxygen buffer using the expression $\Delta IW = -2\log [X_{Fe}/X_{FeO}]$ (e.g., Righter et al., 1997; Wood, 2008), where X_{Fe} and X_{FeO} are the mole fractions of Fe in metal and FeO in the silicate liquid, respectively. ΔIW values calculated for our experiments are from IW-1.8 for Si-free runs down to as low as IW-7.95 for Si-bearing runs (Table 1). If ΔIW is instead calculated with activities, or $\Delta IW = -2\log [a_{Fe}/a_{FeO}]$, where aFe (activity of Fe in metallic liquid) is calculated using the epsilon interaction parameter model for metallic liquids (see Supplementary Material Part 4), and a_{FeO} (activity of FeO in silicate liquid) was calculated using Holzheid et al. (1997), calculated ΔIW values are shifted slightly higher, from IW-1.3 to 7.2 (Table 1). Because most studies utilize the first approach (mole fractions), we include those in the tables and figures, for ease of comparison to previous studies. However, the difference in calculated values using mole fractions and activities is attributable to non-ideality in the Fe-Si system, which should not be ignored; activities are used in all calculations. The range of ΔIW values considered applicable during Earth’s accretion and core formation (e.g., IW-5 to IW-2; Wood et al., 2006; Righter, 2011; Siebert et al., 2011) completely overlaps the range of values calculated here for our experiments.

4.3. Comparison of partition coefficients to previous work

Partition coefficients for the Si-free experiments reported here are between 6.8×10^5 to 2.3×10^6 for Ru which compares closely to previous results at the same or similar conditions reported by Laurenz et al. (2016), Steenstra et al. (2022), and Mann et al. (2012), whose values range from 10^5 to 10^7. Our D(Re) values 2.7×10^5 to 2.5×10^6, are also in close agreement with previous results at the same or similar conditions reported by Righter et al. (2015), Mann et al. (2012), Brenan et al. (2019), and Steenstra et al. (2022), whose values range from 10^5 to 10^7. Our D(Pt) values $\sim 1.3 \times 10^4$, are also in close agreement with the lower range of values for D(Pt) reported by Righter et al. (2015), Mann et al. (2012), Laurenz et al. (2016) and Steenstra et al. (2022), whose values range from 10^4 to 10^6. Finally, our D(Os) values $\sim 3.0 \times 10^4$, are in between values from previous studies at the same or similar conditions (Righter et al., 2015; Yokoyama et al., 2009) from 1.5×10^4 to 2.8×10^5. The slight differences in D(Ru), D(Re), D(Os), and D(Pt) between the various studies is not surprising given the different melt compositions, oxygen fugacities, and metal compositions employed. Similarly, the results for Ti, Nb, and Ta reported here in the experiments with Si-free metallic liquids, are in agreement with results reported by Corgne et al. (2008) and Wade and Wood (2001) and are typically less than 1. Values measured for more reducing conditions are as high as D(Nb) = 4000, and D(Ta) = 1600 (Cartier et al., 2014; Münker et al., 2017). Values for D(Ti) approach 1 at the most reduced conditions (IW-7), similar to the results obtained by Steenstra et al. (2020) for Ti as well.

Partition coefficients from experiments containing Si-bearing metals must be interpreted more carefully due to the strong activity effects of Si in Fe liquids. Partition coefficients at high fO_2 (>IW-2) are expected to be lower than those at low fO_2, with the slope of D versus $\log fO_2$ related to the valence (n) of the element (for positive cations), by a factor of n/4 for each $\log fO_2$ unit (e.g., Capobianco et al., 1999; Righter, 2015; Holzheid and Palme, 1996; Newsom and Drake, 1983). At $fO_2 <$ IW-2, increasing amounts of Si in Fe-Si liquids affects trace metal activities and compositions causing deviations from the D – $\log fO_2$ slopes expected for a specific valence (e.g., Tuff et al., 2011; Righter et al., 2017; Vogel et al., 2018; Steenstra et al., 2020). Thus at low fO_2, the partition coefficients involving FeSi liquids remain lower than expected, but this behavior can be used to better understand partitioning at these low fO_2 conditions. The metal-silicate exchange coefficient of a trace element between metal and silicate melt is constant at fixed T and P, and independent of fO_2 as long as there are no valence changes in the trace metal. In our series at fixed T and P but variable Si content, deviation from the expected value of the metal-silicate exchange coefficient will be used to calculate the activity coefficient for a trace element in FeSi liquids, as will be explained in more detail below.

4.4. Determination of epsilon interaction parameters

Measured metal and silicate compositions were used to calculate metal (met) - silicate (sil) exchange coefficient K_d for Ru, Re, Pt, Os, Ti, Nb, Ta (as well as P, V, Cr, As, Ga, Zn, Pb) according to this reaction:

$$MOn/2_{\mathrm{sil}} + (n/2)Fe_{\mathrm{met}} = M_{\mathrm{met}} + (n/2)\mathrm{FeO}_{\mathrm{sil}} \tag{1}$$

The equilibrium constant of reaction (1) is,

$$\ln K = \ln \frac{\left[a_M^{metal}\right]\left[a_{FeO}^{silicate}\right]^{n/2}}{\left[a_{MO(n/2)}^{silicate}\right]\left[a_{Fe}^{metal}\right]^{n/2}} = \ln \frac{\left[X_M^{metal}\right]\left[X_{FeO}^{silicate}\right]^{n/2}}{\left[X_{MO(n/2)}^{silicate}\right]\left[X_{Fe}^{metal}\right]^{n/2}} + \ln \frac{\left[\gamma_M^{metal}\right]\left[\gamma_{FeO}^{silicate}\right]^{n/2}}{\left[\gamma_{MO(n/2)}^{silicate}\right]\left[\gamma_{Fe}^{metal}\right]^{n/2}} \tag{2}$$

setting $K_d = \frac{[X_M^{metal}][X_{FeO}^{silicate}]^{n/2}}{[X_{MO(n/2)}^{silicate}][X_{Fe}^{metal}]^{n/2}}$ and simplifying further as detailed in Righter et al. (2018) (i.e., assuming that the activity ratios of Fe and M in the silicate melt are constant), the above equations can be re-arranged to yield:

$$\ln K_d = \mathrm{constant} + n/2\ln\gamma_{Fe}^{metal} - \ln\gamma_M^{metal} \tag{3}$$

Combining (3) with $\ln\gamma_M^{metal} = \ln\gamma_{Fe}^{metal} + \ln \gamma_M^0 - \varepsilon_M^{Si} \ln(1-X_{Si})$ and rearranging results in

$$\ln K_d - (n/2 - 1)\ln\gamma_{Fe}^{metal} = \mathrm{constant} - \ln\gamma_M^0 + \varepsilon_M^{Si}\ln(1 - X_{Si}) \tag{4}$$

where γ_{Fe}^{metal} is defined as the activity coefficient of Fe in Fe metal (calculated as described in the Supplementary Material Part 4), γ_M^0 is defined as the activity coefficient of M at infinite dilution, and ε_M^{Si} is an interaction parameter that is used to calculate the activity of a trace metal (M) in Fe-Si liquids (e.g., Lupis, 1983; Righter et al., 2018). ε_M^{Si} is determined directly for each element at 1600 °C, from the slope of “$\ln K_d$ – (n/2 – 1) ln γ_{Fe}^{metal}” versus “$\ln(1-X_{Si})$”.

Interaction parameters, ε_M^{Si}, for Ru, Re, Pt, Os, Ti, Nb, and Ta, were determined by a linear fit to the data, with the standard error (in parentheses below) and the fits passing variance tests in SigmaPlot 12.0. We also derive ε_M^{Si} values for P, Ga, Zn, Pb, V, Cr, As for comparison to previous determinations that used similar methodology to this work (e.

g., Righter et al., 2018; see more detailed discussion of these elements in Supplementary Material, Part 4; Fig. S4). ε_M^{Si} for Re and Ru were determined using a series of 5 experiments each, whereas the Ti, Nb, and Ta and P data were combined from two series of experiments at 1600 °C in MgO capsules. Re and Ru yielded epsilon interaction parameters of 44.9 (7.0) and 44.0(8.0). P, Ti, Nb, and Ta yielded epsilon interaction parameters of 70(15), 10.3(3.2), 45.4(8.0), and 44.8(7.2), respectively (Fig. 2). Finally, epsilon interaction parameters for Re of 49.7(16.9) and for Pt of 28.9(7.6) are within error of those from our Re-only series determination (44.9) and Pt-only series from Righter et al. (2018) (27.4). The value for Os, 42.9(16.4) is the same magnitude as the value we obtained for Ru in the Ru-only series – 44.0(8.0).

4.5. *Comparison to previous work, and the relative effects of S, C, and Si*

For the HSE Ru, Re and Os, our results are the first known to us, whereas many of the other elements can be compared to previous work (Supplementary Material, Part 4). Our values for Ru and Re are similar in magnitude to values measured for Pd, Pt, and Au (Righter et al., 2018). Our P results show good agreement with several previous studies and also confirm the very high and positive epsilon interaction parameter for P in Fe-Si liquids (Righter et al., 2017, 2019). Our newly determined values for Ti, Nb and Ta are lower than previously reported values from the steel making literature (e.g., Steelmaking Data Sourcebook, 1988), but are consistent with results of Steenstra et al. (2020) and with the moderate effects of Si on partitioning that have been observed by us and by Münker et al. (2017) and by Cartier et al. (2014), for example.

All elements studied here have positive epsilon parameters, indicating that dissolved Si causes a decrease in their partition coefficients (Fig. 3). More specifically, D(metal/silicate) for Ti, Nb, Ta, Ru, Re, Pt, and Os will be reduced for all elements with the addition of Si to the metallic liquid. For many elements, dissolved Si has a much greater effect on the activity than C or S (Fig. 3). Furthermore, the effect of Si is much stronger than S for Re, Os, and Ru; Si causes a larger decrease in D (metal/silicate) for Re, Os, and Ru because $\varepsilon^{Si}_{Re,Os,\ or\ Ru} > \varepsilon^{S}_{Re,Os,\ or\ Ru}$ (Fig. 3). Thus the chalcophile behavior expected from some elements will be completely masked by the presence of Si in a metallic liquid.

4.6. *Calculation of activity coefficients in Fe-Ni-Si-C-S liquids*

An activity model using epsilon interaction parameters (Ma, 2001; Wade and Wood, 2005) was previously coded in MATLAB and expanded to include our interaction parameters for Fe-Si liquids (Righter et al., 2017; 2018; 2019). Here we update this model and add our new data for Ru, Re, and Os for a total of 36 elements in Fe-Ni-Si-S-C metallic liquids (Supplementary Material Part 4). Using this model, we demonstrate the large effect of Si on γ, some of which increase by ~1000 (e.g., Re, Pt, Os, Ru) and especially P by nearly 6 orders of magnitude between X_{Si} = 0 and 0.20. In addition, we calculate activities for Fe-S, Fe-C, and Fe-Si systems comparing the effect of each light element on the activity coefficients (Figs. 4 and 5 show Ru, Re, Pt, Os Ti, Nb, Ta; Supplementary Material, Part 4 show all others). In this way the relative effects of each light element can be illustrated, and differential effects on various elements can be evaluated.

Based on the trends in Figs. 4, 5, and S5, some general observations can be made regarding overall behavior of elements considered. Only two elements – Mn and Cr – have activity coefficients that decrease with

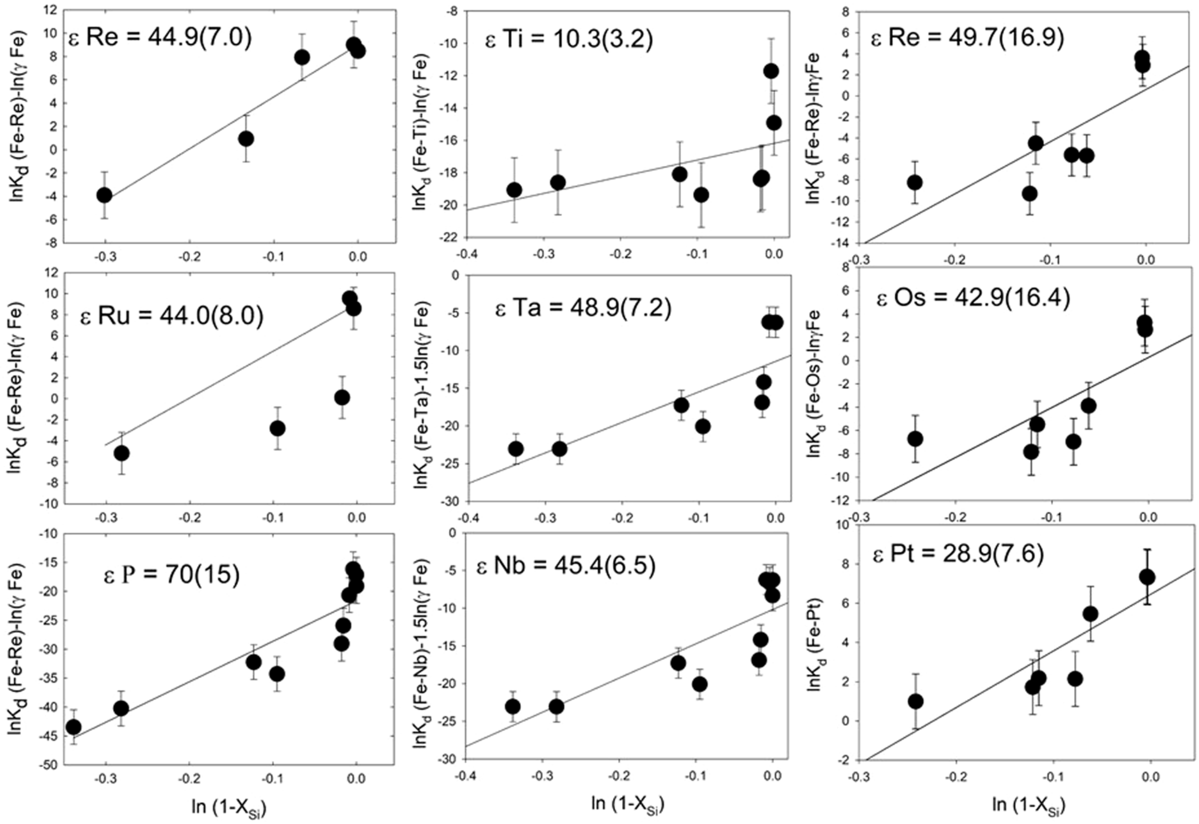

Fig. 2. $\ln K_d$(Fe-Re)–ln(γ_{Fe}), $\ln K_d$(Fe-Ru)–ln(γ_{Fe}), $\ln K_d$(Fe-P)–1.5ln(γ_{Fe}), $\ln K_d$(Fe-Ti)-ln(γ_{Fe}), $\ln K_d$(Fe-Ta)–1.5ln(γ_{Fe}), and $\ln K_d$(Fe-Nb)-1.5ln(γ_{Fe}) versus ln(1-X_{Si}) from the Re- and Ru-series of experiments across a wide range of Si contents in metallic Fe (two left columns). $\ln K_d$(Fe-M) versus ln(1-X_{Si}) from the Re-Pt-Os series experiments (right hand column). The slope of the lines yields the interaction parameter for each – ε_{Re}, ε_{Ru}, ε_{Ti}, ε_{Ta}, and ε_{Nb} - in Fe-Si liquids. In the latter experiment V, Cr, As, Ga, Zn, and Pb were also measured in both metal and silicate and thus calculated ε_{Re}, ε_{Pt}, ε_{Os}, as well as ε_V, ε_{Cr}, ε_{As}, ε_{Ga}, ε_{Zn}, and ε_{Pb} - in Fe-Si liquids; these are presented in the Supplementary Material Part 4.

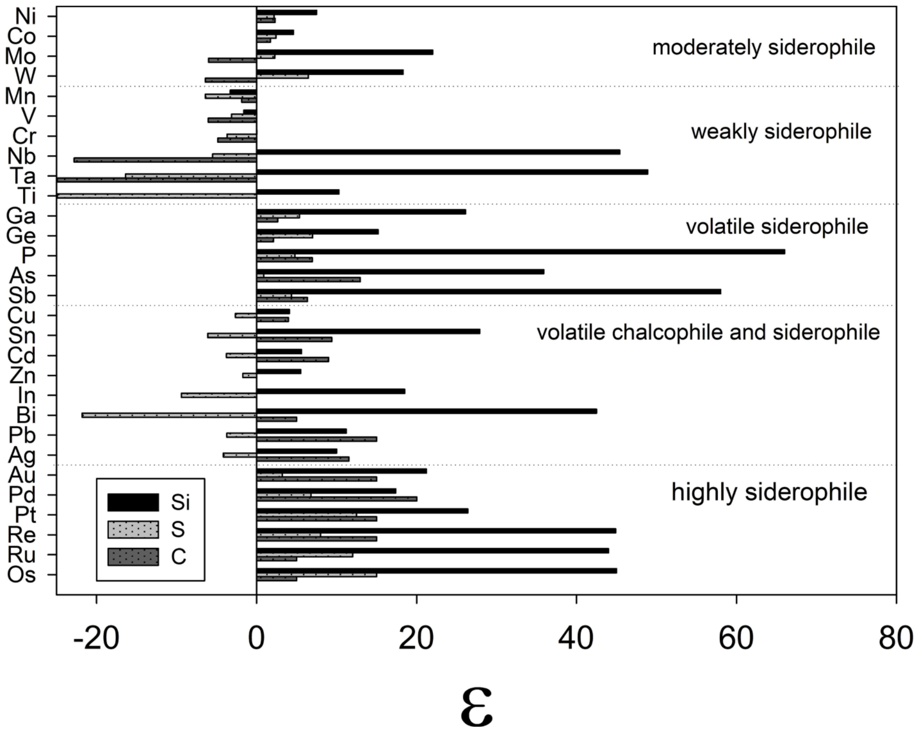

Fig. 3. Comparison of new epsilon interaction parameters for a wide range of elements in Fe-Si, Fe-S, and Fe-C liquids measured in previous studies (Wood et al., 2014; Steelmaking Database, 1988; Righter, 2016; Righter et al., 2017, 2018, 2020). Our new results show that Os, Pt, Re, and Ru all exhibit positive epsilon values for Fe-Si, Fe-S, and Fe-C liquids, with Fe-Si liquid exhibiting larger magnitude values for each element. Ta, Nb, and Ti, in comparison have negative epsilon interaction parameters in Fe-S and Fe-C liquids (favoring a sulfide liquid over an Fe liquid) but exhibit positive epsilon parameters for Fe-Si liquids. The figure is divided into moderately, weakly, volatile, volatile chalcophile, and highly siderophile element groupings to facilitate comparison of the behavior of these groups of elements. Supplementary Material Part 4 also includes a Table of values comparing interaction parameter values from previous work with our new values.

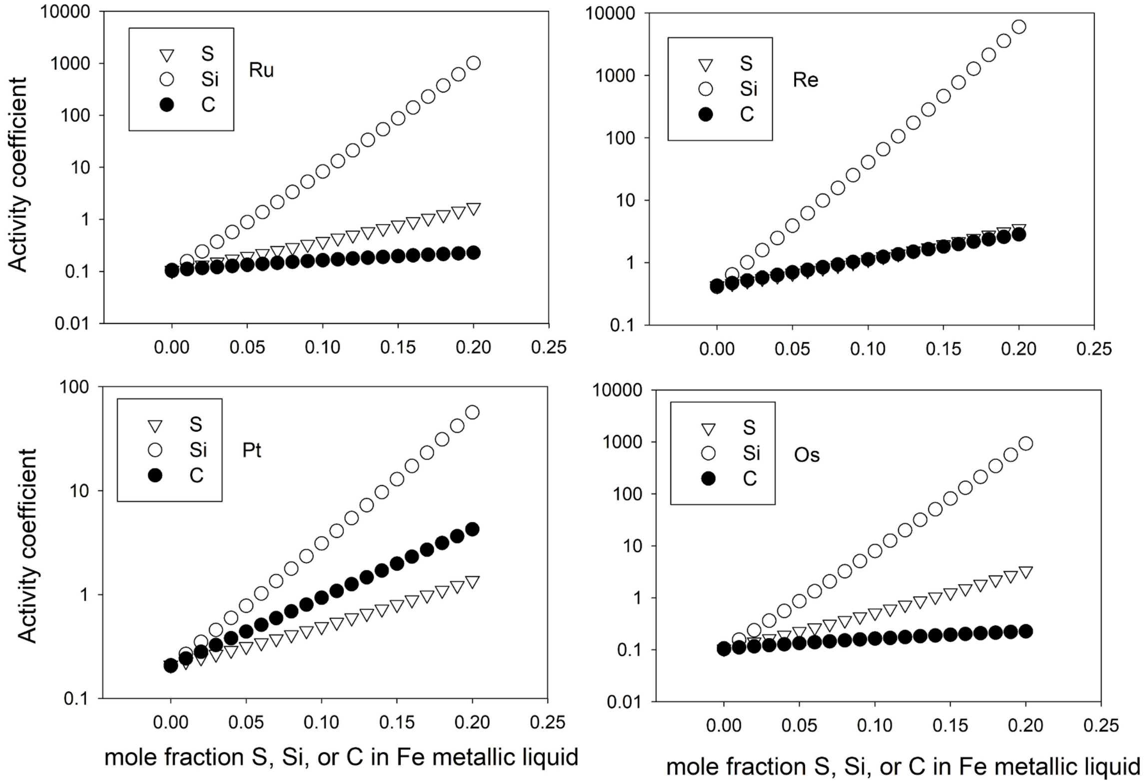

Fig. 4. Variation of activity coefficients for Ru, Re, Pt, Os, in Fe-S, Fe-Si, and Fe-C metallic liquids from X_S, X_{Si}, and $X_C = 0$ to 0.20, illustrating the relative effects of increasing amounts of S, Si, and C on the activity of these four trace elements, at 1873 K. Note that all three S, Si, and C – cause the activity coefficient to increase, which in turn would cause a decrease in the D(metal/silicate). See text for additional discussion.

the addition of all three light elements S, C, and Si, to the Fe metallic liquid. A large group of elements - Ga, Ni, Co, P, Ge, As, Sb, and the 8 HSE – have activity coefficients that increase with the addition of all three elements S, C, and Si, to the Fe metallic liquid. Two elements – Mo and W – have activity coefficients that decrease (i.e., become more siderophile) with the addition of C (but increase with addition of Si and S). The chalcophile elements - Ag, Pb, Bi, Cd, Sn, and Cu – have activity coefficients that decrease (i.e., become more siderophile) with addition

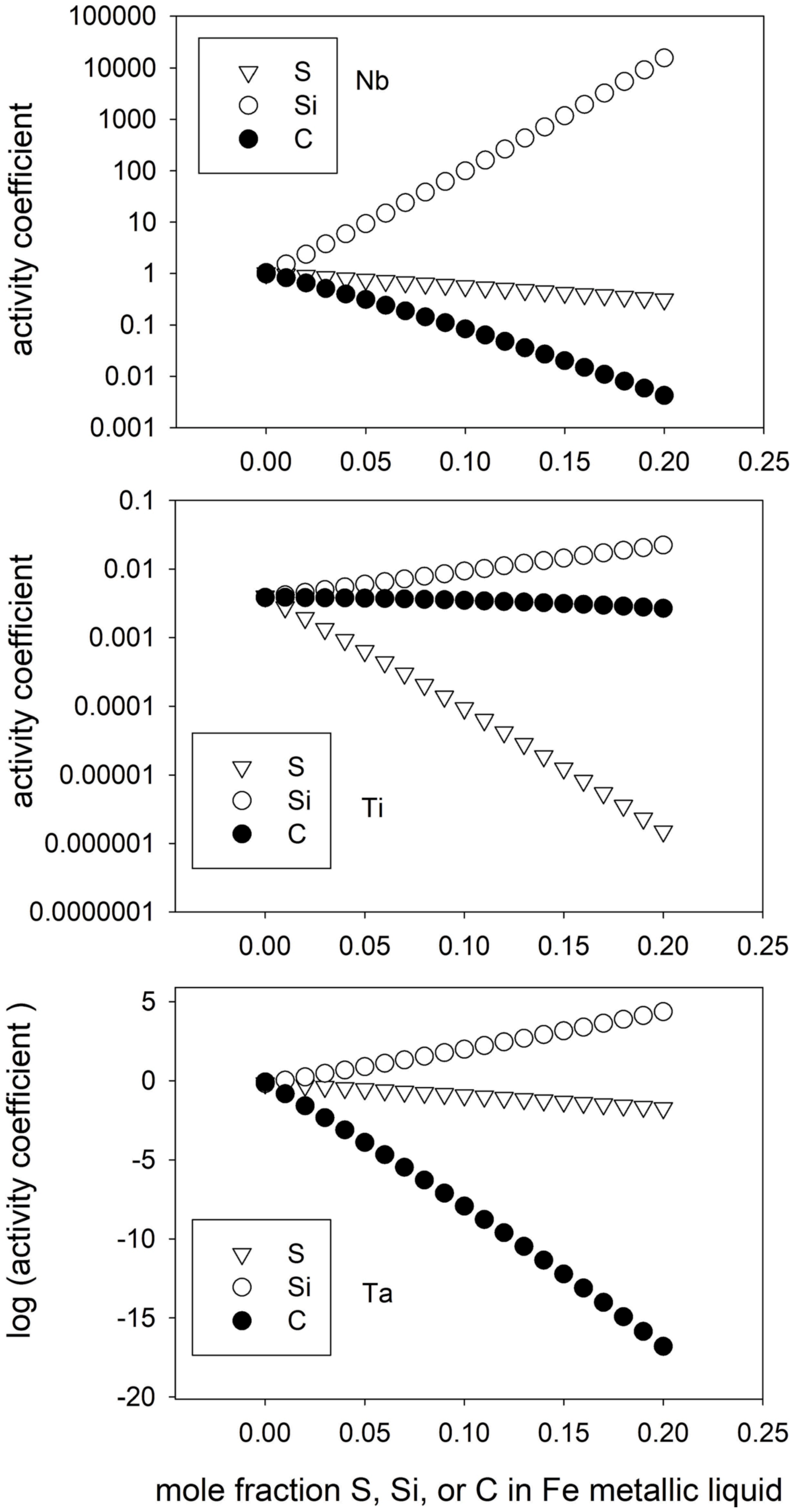

Fig. 5. Variation of activity coefficients for Nb, Ti, and Ta in Fe-S, Fe-Si, and Fe-C metallic liquids from X_S, X_{Si}, and $X_C = 0$ to 0.20, illustrating the relative effects of increasing amounts of S, Si, and C on the activity of these three trace elements, at 1873 K. Note that for all three elements, increasing Si causes an increase in the activity coefficient (thus making Nb, Ti and Ta less siderophile, but that increasing S and C contents cause a decrease in activity activity coefficient (thus making Nb, Ti and Ta more siderophile).

of S (but increase with the addition of Si and C). Finally, In, Zn, Cr, Nb, Ti, and Ta all have activity coefficients that decrease with the addition of both C and S (Si causes increase), thus become more siderophile with the addition of either C or S. It is also worth noting that no elements become more siderophile with only addition of Si; only Mn and Cr are decreased with Si solution in Fe metal, but a decrease is also caused by dissolution of C and S. These general observations very clearly illustrate which elements can become more siderophile with addition of specific elements, and thus are useful guides to understanding effects of both a single element as well as combination of elements. For example, the siderophile tendencies of some chalcophile elements can be cancelled out by dissolution of Si in combination with S (e.g., Bi, Sn, or Cd). Similarly, the affinity of Mo and W for Fe-C metallic liquids will be cancelled out by the dissolution of Si or S in the Fe metallic liquids.

5. Discussion

5.1. *Application to metal/silicate partitioning – comparative core formation in Earth, Mars, and Mercury*

We utilize the newly updated activity model, combine it with partitioning data for multiple siderophile elements, and apply the results to simple accretion and core formation models for Earth, Mars, and Mercury. These three planets are thought to have FeNi metallic cores of significantly different light element compositions with Earth a combination of S, C, and Si, Mars a mixture of S and C, while Mercury has a dominantly Si-rich FeNi core. The activities of the elements, and metal Si, S and C contents, are calculated along hypothetical adiabats during continuous accretion and core formation models. Finally, the calculated planetary mantle concentrations of the elements can be compared to known, measured values for Earth, Mars, and Mercury to evaluate formation models.

5.1.1. *Core compositions of Earth, Mars, and Mercury*

As the terrestrial planets grew during accretion and metal is delivered and intimately dispersed with silicates, there is constant equilibration and re-equilibration of core-forming metal and mantle. For calculations done here, we assume complete equilibrium for these calculations, though some differences will result in assuming partial equilibration. As better understanding of this issue evolves it seems more realistic calculations (e.g., 3D modelling instead of 2D modelling, entrainment of metallic droplets, shear stresses keeping droplets sizes small, etc.) lead to conditions closer to full equilibration (e.g., Deguen et al., 2014; Kendall and Melosh, 2016; Lherm and Deguen, 2018). As the metallic portion grows into a metallic core, the core acquires a light element composition that is specific to the P-T-fO$_2$-composition conditions of the metal-silicate equilibrium. In general, the pressure and temperature at the base of a deepening magma ocean can be approximated by an adiabatic temperature gradient that would depend on the mantle composition and phase equilibria of each specific planet of interest. We calculate metallic liquid composition (S, C, and Si content) along such gradients using the D(S), D(C), D(Si) expressions of Boujibar et al. (2014), Li et al. (2015), and Boujibar et al. (2019), respectively, and mass balance equation $C_{LM}^{M} = C_{LS}^{M}[D_{LM/LS}^{M}]$, where C_{LS}^{M} is given as:

$$C_{LS}^{M} = \frac{C_{bulk}^{M}}{x\left[p + (1-p)D_{SS/LS}^{M}\right] + (1-x)\left[D_{LM/LS}^{M}\right]} \tag{5}$$

where LS stands for 'liquid silicate', LM stands for 'liquid metal', x is the fraction of silicate, p is the fraction of molten silicate, C_{bulk}^{M} is the bulk concentration (by weight) of siderophile element, $D_{SS/LS}^{M}$ is the partition

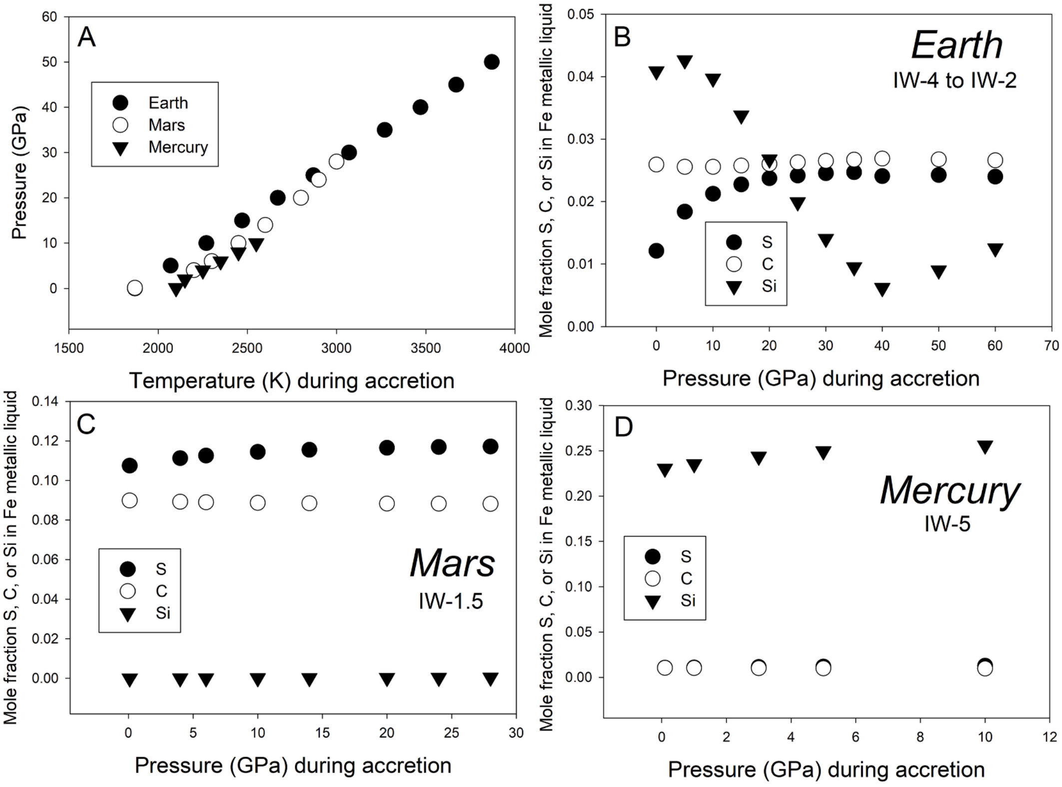

Fig. 6. **A** Variation of pressure and temperature during accretion for Earth, Mars, and Mercury. Adiabatic PT gradients might be typical as accretion proceeds for Earth, Mars, and Mercury. **B, C, D:** evolving core compositions for Earth, Mars, and Mercury (respectively) as accretion proceeds and deepens/ heats. For Earth is the scenario where oxygen fugacity starts near IW-4 and increases during accretion to IW-2 (Fig. 6A), and the metallic liquid composition (X_S, X_C, X_{Si}, and X_{Fe}) changes as accretion proceeds and pressure increases. Similarly, the calculated core compositions are shown for Mars (6C; IW-1.5; mainly S- and C-bearing) and Mercury (6D; IW-5; Si-rich core of 25% Si).

coefficient (by weight) between solid silicate and liquid silicate, and $D^{M}_{LM/LS}$ is the partition coefficient (by weight) between liquid metal and liquid silicate (calculated as described in Section 5.1.3 below). PT gradients for hypothetical magma oceans (Fig. 6**A**) and values of x, p, C^{M}_{bulk} and $D^{M}_{SS/LS}$ (for the light elements S, C, and Si) are tabulated for Earth, Mars and Mercury in Supplementary Material Part 5 (Table S3). The resulting core compositions evolve during accretion and as the magma ocean deepens. For Earth (e.g., Badro et al., 2007; Siebert et al., 2011; Righter et al., 2018), the initially high core Si content decreases at first because the oxygen fugacity (or ΔIW) increases (from −4 to −2) and that is a stronger effect on 4+ Si than the PT effects that cause an increase in the core Si content. However, at higher PT conditions, and where ΔIW has reached values near −2, those PT effects on Si partitioning dominate and that is why the core Si content increases again. The resulting core is a mix of Si, S, and C (Fig. 6**B**). For Mars, the redox conditions and pressures conspire to keep Si out of the core and its core is S- and C-bearing (Fig. 6**C**). For Mercury, the core is Si-rich and C- and S-poor throughout accretion, with a dominantly Si-bearing core of ~25% Si (Fig. 6**D**).

5.1.2. Calculating activities of trace siderophile elements in FeNi metallic liquids

Using the calculated Fe-S-Si-C metallic liquid compositions and PT conditions from Section 5.1.1, activity coefficients for trace siderophile elements can be calculated for each planetary body during accretion. The $\gamma(M)_{met}$ equation has been previously presented and is described in detail in Supplementary Material Part 4. The metallic liquid compositional variation in Si, C, and S causes several orders of magnitude change in the activity coefficient of many trace metals (Fig. 7). For example, the Si-rich core of Mercury results in high activity coefficients for many elements, whereas activities in terrestrial and martian FeNi cores are smaller and similar in most cases (Fig. 7). The elements exhibiting the largest differences in activity coefficients between Mercury and Earth/Mars conditions are P, Bi, Sb, Re where differences are as high as 10^4 to 10^6. This is because the effect of Si is so much greater for these elements than that of S and C (Fig. 7). Elements exhibiting moderate to large differences (100–1000) in activity coefficients between Mercury and Earth/Mars are W, Mo, Ga, Sn, In, As, Os, Ru, and Pt. Most of these are due to strong effects in one element like C (Mo and W) or Si (Ga, Sn, In, As, Os, Ru, and Pt) compared to effects of other light elements. Finally, some elements exhibit a small difference in activity coefficients (≤10) between Mercury and Earth/Mars including Ni, Co, Cu, Nb, Cr, Mn, V, Cd, Zn, Ag, Pb, Au and Pd. In these cases the small difference is attributed to moderate effects that are canceled out such as chalcophile elements that are also silicophobic, or simply those elements that have very small interaction coefficients regardless if they are positive or negative. These 27 elements illustrate the range of activity variations expected for the terrestrial planets; several specific applications will be highlighted in the next section.

5.1.3. Calculating D(metal/silicate) for FeNi metallic liquids and resulting mantle concentrations

Application of our new activity model to some specific examples for Earth, Mars and Mercury allows us to calculate concentrations of trace siderophile elements in the liquid mantle after core formation. Concentrations of siderophile elements in the liquid mantle, or C^{M}_{LS}, are calculated using equation (5) above, and the values of x, p, C^{M}_{bulk} and $D^{M}_{SS/LS}$ (for the trace elements instead of light elements S, C, and Si) tabulated for Earth, Mars and Mercury in Supplementary Material Part 5 (Table S3). Equation (5) also requires predictive expressions for the trace element metal/silicate partitioning, where $D^{M}_{LM/LS}$ is calculated using:

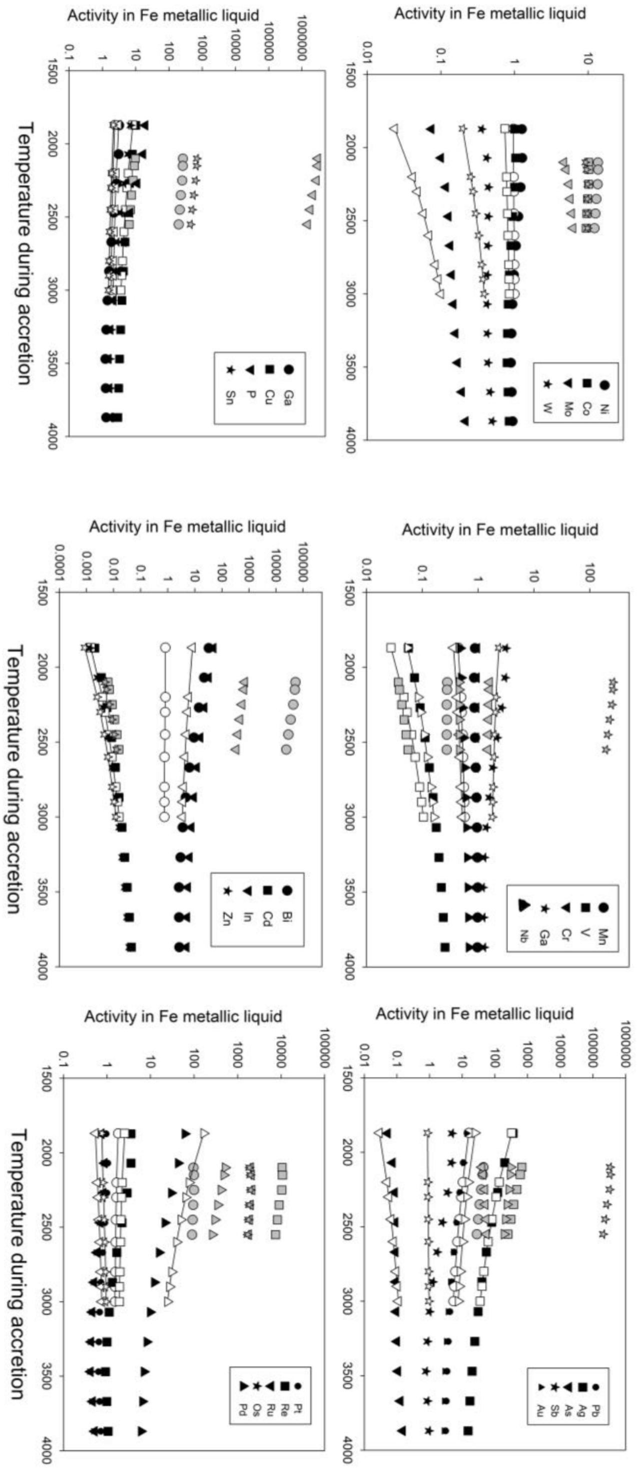

Fig. 7. Variation of activity coefficients for 27 elements in the activity model as accretion proceeds along adiabatic PT gradients from Fig. 6, for Earth (solid symbols), Mars (open symbols), and Mercury (gray symbols). Panel A shows moderately siderophile elements Ni, Co, Mo, and W. Panel B shows volatile siderophile elements Ge, Cu, P, and Sn. Panel C shows weakly siderophile elements Mn, V, Cr, Ga, and Nb. Panel D shows volatile chalcophile elements Bi, Cd, In, and Zn. Panel E shows chalcophile elements Pb, Ag, As, Sb, and Au. Panel F shows highly siderophile elements Pt, Re, Ru, Os, and Pd. The largest differences between the Fe metallic liquid compositions in Fig. 6B (i.e., Mercury versus Mars or Earth) are shown by P, Bi, Sb, and Re. Intermediate effects are shown by W, Mo, Ga, Sn, In, Au, Os, Ru, and Pt. Small to moderate differences are exhibited by Ni, Co, Cu, Nb, Cr, Mn, V, Cd, Zn, Ag, Pb, Au and Pd.

$$\begin{aligned}\ln D'^{M}_{LM/LS} &= \ln D^{M}_{LM/LS} + \ln(\mathrm{M})\mathrm{met} \\ &= \mathrm{alnfO_2} + \mathrm{b/T} + \mathrm{cP/T} + \mathrm{d(nbo/t)} + \mathrm{e} \end{aligned} \qquad (6)$$

where $D'^{M}_{LM/LS}$ is a partition coefficient that has been recalculated to take into account the activity of the trace metal of interest, $\ln D^{M}_{LM/LS} + \ln\gamma(\mathrm{M})_{\mathrm{met}}$. Thus, the partition coefficient expression becomes $\mathrm{alnfO_2} + \mathrm{b/T} + \mathrm{cP/T} + \mathrm{d(nbo/t)} + \mathrm{e} - \ln\gamma(\mathrm{M})_{\mathrm{met}}$. The regression coefficients (a through e) used in Equation (6) are derived for Re, Pt, Os, Ru, Mo, W, and Ti by multiple linear regression of published partition coefficient data. Although we have derived regressions for these analysis in previous work, many significant new contributions have been published and those are combined with previous work to derive updated regressions coefficients (see detailed discussion and information in Supplementary Material, Part 6, Fig. S6).

5.2. Ru, Re, Pt, Os, Mo, and W contents of mantles during Earth accretion

By combining the activity variations due to the changing metal composition during accretion, with pressure, temperature, fO_2, and melt compositional effects on D(metal-silicate) (Equation (6), the mantle abundances of these elements resulting from metal-silicate equilibrium can be calculated in two fO_2 scenarios for the deep early molten Earth (Equation (5). Previous work has shown that Earth's mantle abundances of Ni, Co, Mo, W, P, Mn, V, Cr, As, Sb, In, Ge, Ga, Zn, Bi, Cu, Cd, and Pb, can be explained by metal-silicate equilibrium near 50 GPa, 3800 K, in an accretion scenario with variable fO_2, and resulting in a Si-rich core (Righter et al., 2016, 2017, 2018, 2019; Siebert et al., 2013; Bouhifd and Jephcoat, 2011; Fischer et al., 2015). We will examine the effect of Earth

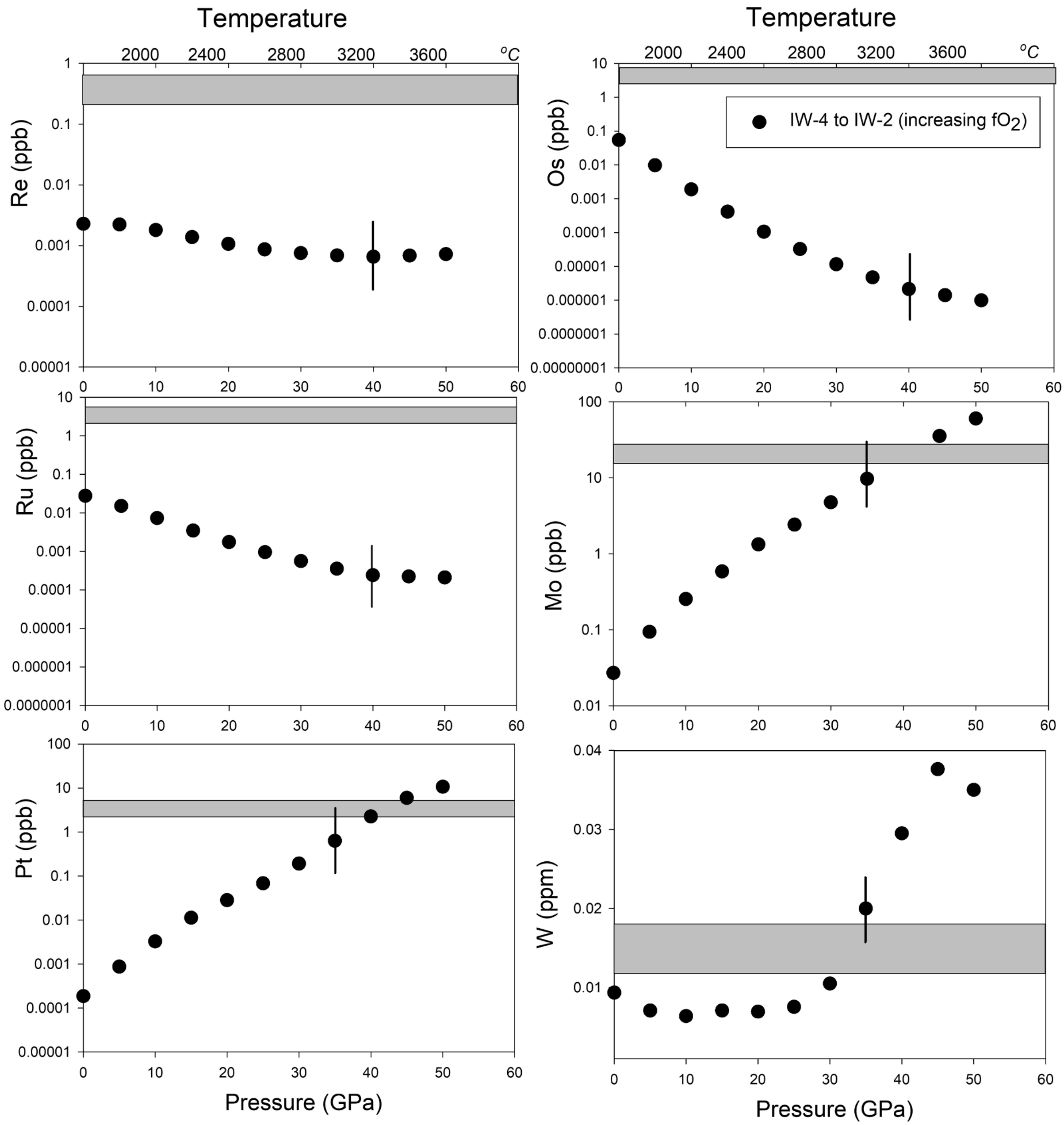

Fig. 8. Variation of Re, Ru, Pt, Os, Mo, and W concentrations in an evolving magma ocean as terrestrial accretion proceeds, with fO_2 changing from near IW-4 early to IW-2 late. The phase equilibria of Fiquet et al. (2010) are used to guide the PT path for melting. Horizontal shaded regions are primitive mantle estimates (from Palme and O'Neill, 2014). Note that while Mo, W, and Pt approach values similar to the BSE estimates for Earth, Re, Ru and Os all become orders of magnitude lower, thus requiring the addition of material in late accretion or a late veneer (see text for discussion).

accretion upon three aspects of mantle geochemistry: Re/Os, Pt/Os and Os isotopes, Mo and Ru isotopes, and Mo/W.

5.2.1. Re/Os, Pt/Os and Os isotopes

HSE concentrations in an early deep magma ocean have been studied by a number of previous works (Mann et al., 2012; Holzheid et al., 2000; Righter et al., 2008; Bennett et al., 2016). Au, Pd and Pt become higher than observed in Earth's mantle (Righter et al., 2018), and ultimately require a process that removes them from the mantle. Our new results for Pt are nearly identical to the previous work (Righter et al., 2018) and support the recent conclusions of Suer et al. (2021) who confirmed the high Pt solubilities in deep silicate melts as well; the latter study also argues for a removal process to bring the post core formation Pt concentrations to levels commensurate with current mantle concentrations. With the new results including more accurate effects of FeSi liquids than previous efforts (e.g., Righter et al., 2015, 2018), Ru, Re, and Os can be added to the modelling. Modeled mantle Re, Os, and Ru abundances are all far lower than estimates of terrestrial BSE concentrations (Fig. 8). The extremely low concentrations of Re, Os, and Ru at the end of accretion (or at least at the depth range that explains most other siderophile elements) means that some additional source is required to bring the concentrations up to the higher levels of the BSE, such as a late veneer or late accretion (Mann et al., 2012; Holzheid et al., 2000; Laurenz et al., 2016; Righter et al., 2018), or trapping of some small fraction of metal in the post core-formation mantle (e.g., Jones and Drake, 1986; Wang and Fei, 2023). However, here (and below) we focus on the implications of this early metal-silicate equilibrium for Os isotopes.

A deep magma ocean would have distinctive compositional traits that will be critical to understanding potential fractionation of Re/Os and Pt/Os. As the magma ocean deepens to 50 GPa, the Re/Os ratio of the silicate melt changes from values of ~0.1 to 10 (Fig. 9**A**). These values indicate that any of this early liquid that gets trapped in the mantle will attain higher ^{187}Os/^{188}Os relative to chondritic values due to the decay of ^{187}Re. Across the same depth range, the Pt/Os ratio increases substantially over this timeframe from values as low as 0.001 to ~10^7 (Fig. 9**A**). In contrast to Re/Os, these high Pt/Os ratios indicate that any of this early liquid that gets trapped in the mantle (e.g., Labrosse et al., 2007) could become very radiogenic in ^{186}Os due to the

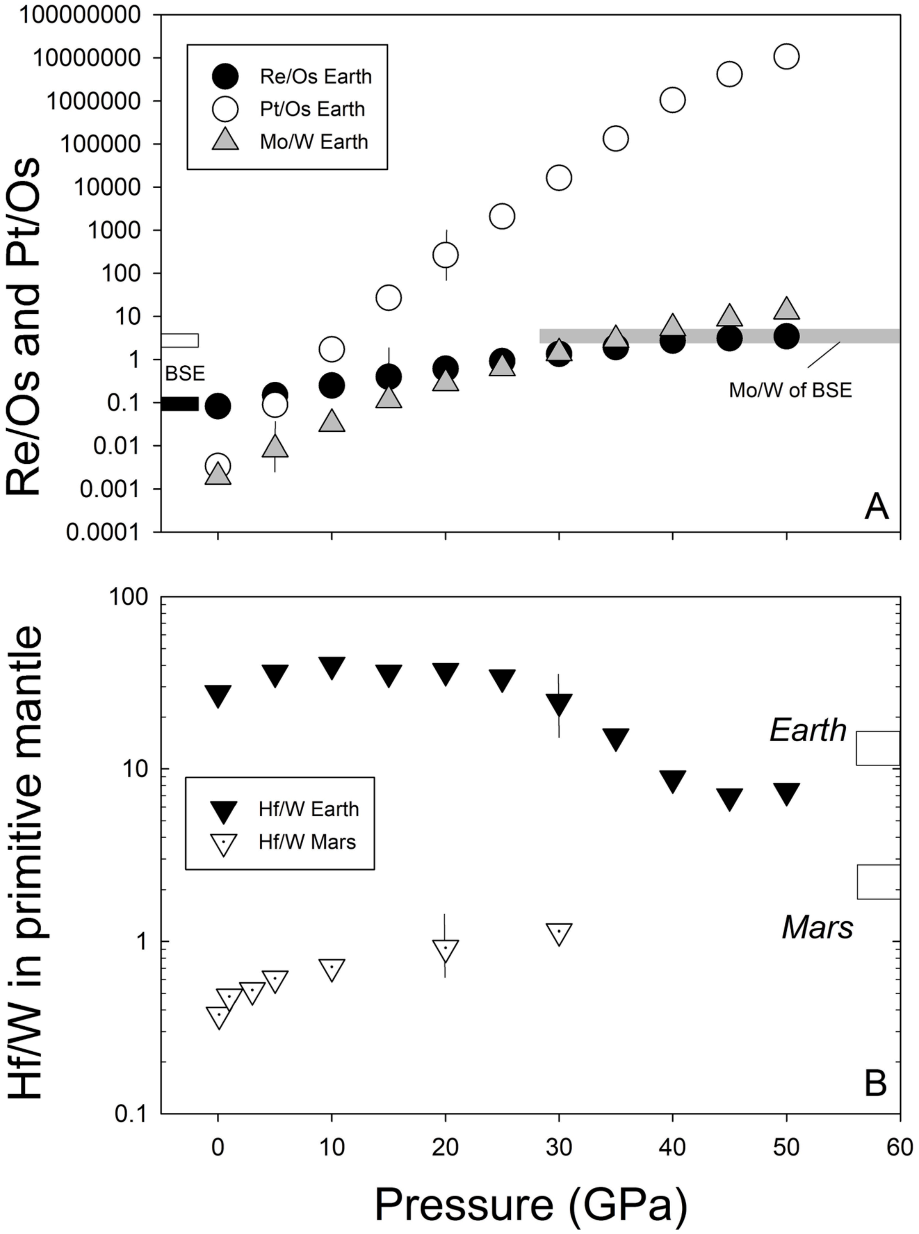

Fig. 9. **A:** Evolution of Re/Os, Pt/Os, and Mo/W in magma ocean in the same model presented in Fig. 8. The Re/Os and Mo/W ratios increase modestly, while the Pt/Os ratio becomes higher by several orders of magnitude. This illustrates the potential for generating ^{186}Os enriched portions of the mantle from decay of ^{190}Pt. early in Earth's accretion and differentiation history. ^{186}Os (derived from Pt decay) and ^{187}Os (derived from Re decay) would thus be decoupled in looking for this early differentiation signature. In addition, the Mo/W ratio of the BSE can be achieved by metal-silicate equilibrium at pressures near 35–40 GPa during Earth accretion and growth, and does not require any special chemical additions such as late S-rich accretion. Mo, W, Re, Pt, and Os values from Palme and O'Neill (2014). Fig. 9**B:** Hf/W in silicate Earth and Mars during accretion. Earth's silicate fraction easily achieves Hf/W at the base of a 35–40 GPa magma ocean. In contrast Mars' silicate fraction does not achieve values > 1 at the pressure range favored for core formation models, yet the bulk silicate Mars has Hf/W near 2. This weak leverage of core formation on the Hf/W ratio suggests an important role for silicate fractionation of Hf/W and in the generation of W isotopes anomalies in Mars. Representative error on calculated concentrations are shown in both (A) and (B) for several points.

decay of ^{190}Pt. Such trapped material could evolve to radiogenic ^{186}Os/^{188}Os ratios that would be indicative of ancient material, while also coupled with radiogenic ^{187}Os/^{188}Os. Measurements of elevated ^{186}Os/^{188}Os ratios in plume magmas show both correlated and uncorrelated variations in ^{186}Os/^{188}Os and ^{187}Os/^{188}Os ratios (Walker, 2009; Ireland et al., 2011). Similar observations have been attributed to ancient crust (Day et al., 2017; Day and Driscoll, 2019), but they might also be due to ancient trapped mantle heterogeneities as has been observed in other plume samples and using other isotopic systems such as W, Nd, and Pt (e.g., Rizo et al., 2019; Touboul et al., 2012; Mundl-Petermeier et al., 2020; Creech et al., 2017). Indeed, the early magma ocean liquids would have the high Pt/Re ratios (>100) required to explain some of the higher ^{186}Os/^{188}Os ratios measured in the Kea-trend Hawaiian samples (Ireland et al., 2011). Although these early liquids clearly have potential to develop high ^{186}Os/^{188}Os and ^{187}Os/^{188}Os ratios, they also have extremely low Os concentrations, and imparting that isotopic signature onto the surrounding "normal" mantle with higher Os contents will be a challenge. If such ancient trapped liquids are responsible for the highly radiogenic plume (e.g., Hawaiian) signatures, simple mixing constraints require that they dominate the source of the plume melts as a major component, not a minor one.

5.2.2. Ru and Mo isotopes

Recent studies of Ru and Mo in planetary materials have revealed a dichotomy in the meteoritic materials that represent the inner solar system. The carbonaceous chondrite (CC) and non-carbonaceous chondrite (NC) source materials were recognized from Cr and Ti isotopes (e.g., Warren, 2011; Dauphas et al., 2014) recently extended to Mo and Ru (Budde et al., 2019; Hopp et al., 2020; Worsham et al., 2019; Bermingham et al., 2018). Because Ru isotopes are commonly considered with Mo, and form a correlation (e.g., Dauphas et al., 2004; Hopp et al., 2018, 2020; Worsham et al., 2019; Bermingham et al. 2018), here we revisit Ru and Mo by using our new results for Ru and updated regressions for Ru and Mo. This new approach specifically allows the effects of Si to be accounted for both elements.

The updated Mo expressions yield a very similar result to that of Righter et al. (2016) where Mo contents were attained during the main phase of accretion (Fig. 8) and would thus be representative of the materials that formed the main accretion stage of Earth. In contrast, the very low Ru resulting from accretion and metal-silicate equilibrium (Fig. 8) means that the Ru observed in BSE must have been added late. Thus, the isotopic composition of Ru will be a good indicator of late accretion source materials (also supporting the conclusion of Dauphas et al., 2004).

Because the Ru isotopic composition of the BSE is very similar to enstatite chondrites, Fischer-Gödde and Kleine (2017) suggested that the late veneer is dominated by inner solar system material. However, Budde et al. (2019) showed that the Mo isotopic composition of the BSE is a mixture of NC and CC contributions, and Fischer-Gödde et al. (2020) argued that late accreted materials could have been CC-like based on mass independent Ru isotopic compositions of Eoarchean samples from Isua, Greenland. Finally, Hopp et al. (2020) show that the Mo and Ru isotopic data could be explained if both the late veneer and Moon-forming are a mix of NC (or enstatite chondrite) and CC material. Whether the late additions are a mix of CM + EH (e.g., Greenwood et al., 2018) or a mix of NC + CC (Budde et al., 2019; Hopp et al., 2020), our partitioning data support the concept of Mo representing main and later stages of terrestrial accretion and Ru the latest stages of accretion. Even if Mo was added late, its BSE concentration was established during the main phase of terrestrial growth, and a late veneer (~1% of Earth mass) comprised of 0.8 EH and 0.2 CM (for example) would add too little Mo to the Earth to meaningfully change the Mo abundance. Overall this supports the conclusion of Dauphas (2017) and shows that it is robust for the scenario of a core forming multi-component Fe-Ni-Si-S-C metallic alloy.

5.2.3. Mo/W ratio

The terrestrial Mo/W ratio is sometimes invoked to argue the need for late sulfide segregation into the core (e.g., Wood et al., 2014; Jennings et al., 2021). With our updated expressions, and ability to model Fe-Ni-Si-S-C liquids, the known effects of these light elements can be quantified. Our modelling shows that the BSE Mo/W value of ~3.9 can be achieved by simple metal-silicate equilibration during accretion, where the metallic liquid re-equilibrates with liquid mantle as PT conditions increase (Fig. 9**A**). The values of BSE are attained in the PT interval near 35–40 GPa, which is the depth range proposed in some previous studies. This would not require any special scenario of a sulfide-rich segregation event later in accretion. The difference from previous modelling may be due to the current assessment including the combined effects of all three Si, S, and C, rather than focusing on C (Huang et al., 2021) or S and C (Wade et al., 2012).

5.3. Martian mantle Hf/W geochemistry imparted by core formation

The updated partitioning expression for D(W) can also be applied to understanding the martian mantle Hf/W value, which has been used to place constraints on the timing and conditions of martian core formation (Brennan et al., 2020; Dauphas and Pourmand, 2011; Righter and Shearer, 2003). Because the martian core is smaller, the fO_2 slightly higher and the PT conditions slightly lower compared to Earth, and a more refractory element enriched bulk martian composition (e.g., Taylor, 2013), the martian Hf/W ratio is significantly lower than that of the Earth and Moon (2–5, compared to 12–20 for Earth; Fig. 9**B**). Modelling of the Hf/W ratio using our Mars core modelling from Section 5.1 shows that this value remains low during core formation (~1.0), similar to the constraints provided by martian meteorites (~2; Taylor, 2013). As a result, this low Hf/W ratio (Fig. 9**B**) caused by core formation leaves a post core formation martian mantle with only weak leverage on generation of ^{182}W anomalies. However, the silicate differentiation of Mars has left its elemental and isotopic fingerprint on martian mantle reservoirs (Foley et al., 2005; Kruijer et al., 2017; Debaille et al., 2009; Lapen et al., 2010, 2017). These latter models require fractionation of Sm/Nd, Lu/Hf, and Re/Os caused by deep and early silicate fractionation at the base of a magma ocean. Thus it is more likely that the ^{182}W anomalies in the martian mantle (e.g., +0.5 to +1.8 in shergottites; Kruijer et al., 2017 and +2 to +3 for nakhlites; Foley et al., 2005; Lee and Halliday, 1997) are caused by the significant and known fractionation of Hf and W caused by most silicate phases during melting (e.g., Righter and Shearer, 2003). Modelling of the ^{182}W anomalies should consider Hf/W fractionation within the silicate fraction as well, and coordinate modelling with other isotope systems (e.g., Zr) which might provide additional constraints on timing (Iizuka et al., 2016; Haba et al., 2021).

5.4. Conditions of Mercury core formation from MESSENGER data

Mercury is thought to be the most reduced terrestrial planet with its large metallic core (e.g., Smith et al., 2012) and perhaps even a sulfide layer at the base of the mantle (Namur et al., 2016). Because Ti becomes siderophile at very reducing conditions, Ti may be a good indicator of the redox conditions during core formation on Mercury. Cartier et al. (2020) argue that Ti contents at the surface of Mercury are consistent with core formation and do not require the existence of a sulfide layer in the interior of Mercury. The work of Cartier et al. (2020) is a sound and substantial contribution and allows consideration of this fundamental aspect of Mercury's differentiation. The general question of Ti distribution within Mercury can be reconsidered here, because we now have measured the specific effect of Si – a major element in Mercury's core - on the activity of Ti in Fe metallic liquids, which was not possible in previous studies.

Mercury's core size, coupled with bulk composition models, and surface Ti data allow an estimate of redox conditions of core formation. Using CM, EH and CB chondritic compositions to illustrate the effect of bulk composition (since Ti content of the chondritic building blocks will be a fundamental control on any surficial Ti content), assuming Ti is incompatible during mantle melting (D(Ti) mantle/melt = 0.01; Wang et al., 2019), and considering the range of estimates of core size fraction for Mercury (0.69 to 0.77), we calculate the magnitude of D(Ti) required to explain the Ti/Al (Ti contents of ~280–350 ppm) at the surface (Fig. 10**A**). For comparison, we calculate the value of D(Ti) as a function of fO_2, using a predictive expression derived as above using source data compiled in Supplementary Material Part 6. P and T are fixed at values near the core-mantle boundary (e.g., Hauck et al., 2013) – 5.5 GPa and 2300 K, with NBO/T fixed at a value of 3.0, and activity is calculated for the Fe-Si liquid. The effect of Si will increase the activity coefficient for Ti, and thus make Ti less siderophile, putting more Ti into the mantle. Given this anticipated effect, it is possible the subchondritic Ti/Al ratio measured by MESSENGER (Cartier et al., 2020) could be difficult to explain by core formation, even at reducing conditions, because the D (Ti) metal/silicate will remain low.

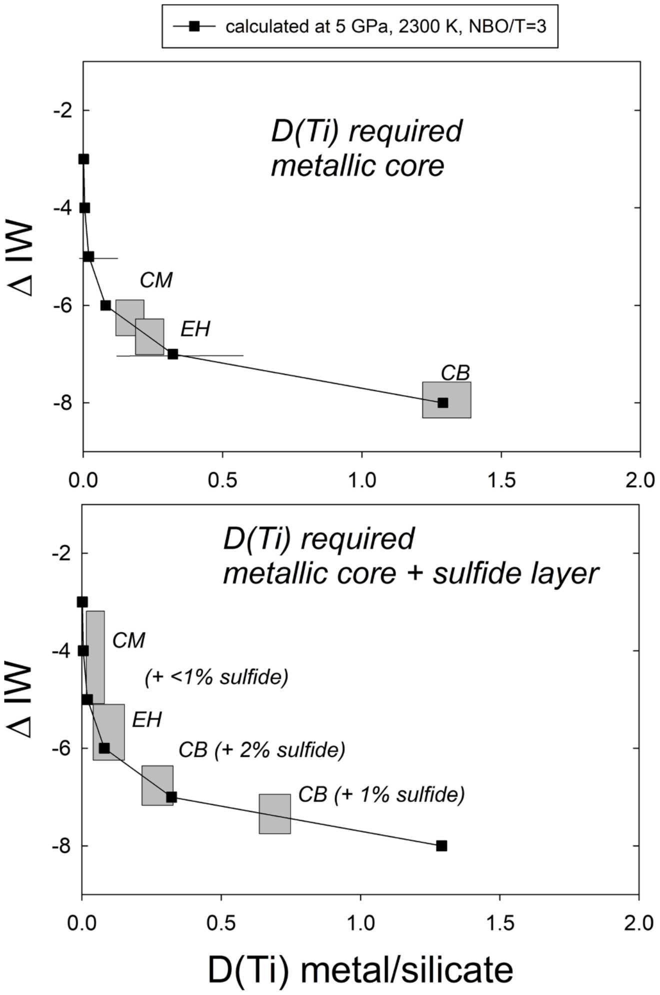

Fig. 10. Constraints on fO_2 of Mercury core formation based on Ti partitioning for scenarios with metallic liquid (A) and metallic liquid and sulfide (B). (A) If Mercury bulk composition is that of CM or EH chondrites, segregation of a metallic core at ΔIW ~−6 to −6.5 would explain the Ti content observed in the crust of Mercury (based on Ti/Al = 0.035; Cartier et al., 2020). Small differences in core size (77% versus 69%) are represented by the width of the shaded boxes; Ti behaves incompatibly D(mantle/melt = 0.01; Wang et al., 2019) and the calculation assumes a molten mantle with a melt fraction of 20%. If Mercury is made of CB chondrite-like material, the D(Ti) metal/silicate required is higher and corresponds to values at ΔIW = −8.0, at the low end of range of estimates for the interior of Mercury. (B) Because D(Ti) sulfide/silicate is much higher than D(Ti (metal/silicate) sulfide could easily sequester Ti more efficiently than metal. In such cases, the D(Ti) metal/silicate required to explain the Ti/Al values would be lower than the metal only examples shown in (A). To illustrate the role of sulfide, our calculations assume a D(Ti) sulfide/melt ~50 (see studies of Namur et al., 2016; Boujibar et al., 2019, 2020; Steenstra et al., 2020). Even with a small amount of sulfide crystallizing out of the molten mantle (<1%) would require a much lower D(Ti) metal/silicate with both the CM and EH bulk compositions and allowing core formation to occur at IW-4 to IW-6. In the case of a CB bulk composition, the fractionation of 1% to 2% sulfide would allow the Ti/Al to be satisfied at IW-6 to IW-7.5, slightly higher fO_2 than for the "metal only" case illustrated in A. For both (A) and (B) the values of D(Ti) metal/silicate are calculated at 5.5 GPa, 2300 K, NBO/T = 3, and gamma Ti in FeSi liquids as described in the Supplementary Material, part 4. Representative error on calculated D(Ti) is shown in (A) for several points.

The calculated D(Ti) values at Mercurian core-mantle boundary conditions (5.5 GPa, 2300 K, NBO/T = 3.0, and gamma Ti in FeSi liquids) overlap the range of modelled Ds required to explain the surface Ti contents, at values near IW-6 to IW-6.5 (Fig. 10**A**). If Mercury is CB-like in bulk composition, the D(Ti) metal/silicate required are higher and at a lower fO_2 (IW-7.5). Thus core formation appears to explain the Ti content at the surface of Mercury, whether Mercury is made of CM-, EH-, or CB-like chondritic material. However, because Ti is even more compatible in sulfide than it is in metal, a small amount of sulfide fractionation could lower the D(Ti) metal/silicate required during core formation, thus allowing solutions at higher fO_2 (Fig. 10**B**). For CM or EH compositions, the surface Ti/Al content can be explained by core formation at IW-4 to IW-6 with even a small (<1%) sulfide fractionation, and for a CB composition, the Ti/Al content can be explained by core formation at IW-6 to IW-7.5 with 2% or 1% sulfide fractionation, respectively. Sulfide fractionation might be more realistic at the higher fO_2 range where sulfide saturation can occur at lower melt S contents (1–2 wt% S; Malavergne et al., 2014) compared to lower fO_2 (8–10 wt% S; Malavergne et al., 2014). Mercury's surface Ti/Al content can thus be explained by either metallic liquid or metallic + sulfide liquid segregation, depending on Mercury's bulk composition and the oxygen fugacity. These interesting results based on Ti should be explored in more detail and could be combined with Cr and other lithophile/siderophile elements to place even more stringent constraints on Mercury's formation fO_2.

6. Summary

Epsilon interaction parameters for Ru, Re, Pt, Os, Nb, Ta, and Ti have been determined for FeSi alloys at 1600 °C and 1 GPa. These new values demonstrate that Si has a substantial effect on the magnitude of the activity coefficients for all seven elements. In addition, we determine epsilon interaction parameters for V, Cr, As, Pb, Ga, and Zn that are in agreement with previous studies (Righter et al., 2017, 2018). Nb should be explored in more detail because its interaction parameter determined here is much different than a previous study; resolving the magnitude of the parameter will be important to a full understanding of Nb geochemistry. We present an updated epsilon interaction parameter model that allows calculation of activity coefficients for 27 trace siderophile elements in Fe-S-C-Si liquid systems. This new model is then used to compare behavior for various elements and calculate activity coefficients for siderophile elements during core formation in Earth, Mars and Mercury.

Earth's mantle concentrations of Pt, Mo, and W approach BSE at the conditions of a deep magma ocean, whereas Ru, Re, and Os concentrations are lowered to very low levels and require addition of material to bring the concentrations of Ru, Re, and Os to the higher levels observed in the BSE. Ru and Mo isotopes reinforce this scenario – Mo was established by metal-silicate equilibrium during main stage of accretion and core formation, while Ru was established by late addition of material that could have been a mix of CM + E or NC + CC. The high Pt/Os and Re/Os ratios in the post core formation terrestrial mantle could lead to isolated portions that acquire $^{186}Os/^{188}Os$ and $^{187}Os/^{188}Os$ enrichments; the coupled Os isotopic values may be a useful signature of ancient mantle material. Finally, the terrestrial Mo/W value can be achieved during the main stage of accretion and core formation without late addition of special sulfur-rich material. This reflects the combined effects of light elements Si, S, and C on the activity of Mo and W during accretion.

Mars accreted and differentiated quickly as constrained by isotopic studies (Nimmo and Kleine, 2007; Dauphas and Pourmand, 2011; Tang and Dauphas, 2014). However, its low mantle Hf/W ratio measured in martian meteorites, and calculated in core formation models, is difficult to reconcile with the sizable W isotope anomalies in martian materials. Instead, the anomalies can more easily be explained by silicate fractionation of Hf/W that is expected in the deep mantle differentiation constraints by other isotopic systems (Nd, Hf, Os; Righter et al., 2020; Righter and Shearer, 2003).

The fO_2 prevailing during the formation of Mercury can be constrained by the distribution of Ti between core and mantle. Our results show that the Si-rich core expected for Mercury would make Ti even less siderophile than a Si-free core. Even with this reduction in siderophile nature, the Ti content of the mantle is consistent with control by core formation, with a D(Ti) near 0.2, and for a wide range of chondritic bulk compositions – CM, H, and EH. For a CB bulk composition, Ti contents could be explained by metal segregation (core formation) or a combination of metal and sulfide segregation. A combined assessment of Cr and Ti may offer the strongest constraints on the fO_2 of Mercurian core formation.

Declaration of Competing Interest

The authors declare that they have no known competing financial interests or personal relationships that could have appeared to influence the work reported in this paper.

Acknowledgements

This work was supported by an RTOP from the NASA Cosmochemistry program to KR, and directed research for NASA Planetary Science Division. A portion of this work was performed at the National High Magnetic Field Laboratory, which is supported by the National Science Foundation Cooperative Agreement No. DMR-1644779 and the state of Florida. We thank A. Peslier and K. Ross for their assistance with electron microprobe analysis at JSC. LA-ICP-MS analysis at FSU was supported by NASA grants to MH. Journal reviews of C. Jackson and R.J. Walker are much appreciated and led to marked improvements to the manuscript. We thank H. Helmy for editorial handling, and K. Iacovino, G. Moore, K. Prissel, and F. McCubbin for many fruitful discussions.

Appendix A. Supplementary material

The Supplementary Material file contains additional information (figures, tables, and text) about electron microprobe analysis (Part 1: sample homogeneity and treatment of HSE interferences), LA-ICP-MS analysis (Part 2: comparison of standards data), sample textures (Part 3: back scattered electron images of many run products from each series), activity modelling (Part 4: comparison of epsilon interaction parameters and the full activity model equations), assumptions used in core formation modelling (Part 5: bulk planetary traits), and metal/silicate partitioning regression analysis (Part 6: equations and comparisons of predicted and measured partition coefficient values). Supplementary material to this article can be found online at https://doi.org/10.1016/j.gca.2023.06.014.

References

Armytage, R.M.G., Georg, R.B., Williams, H.M., Halliday, A.N., 2012. Silicon isotopes in lunar rocks: Implications for the Moon's formation and the early history of the Earth. Geochim. Cosmochim. Acta 77, 504–514.

Asanuma, H., Ohtani, E., Sakai, T., Terasaki, H., Kamada, S., Kondo, T., Kikegawa, T., 2010. Melting of iron–silicon alloy up to the core–mantle boundary pressure: implications to the thermal structure of the Earth's core. Phys. Chem. Miner. 37, 353–359.

Badro, J., Fiquet, G., Guyot, F., Gregoryanz, E., Occelli, F., Antonangeli, D., d'Astuto, M., 2007. Effect of light elements on the sound velocities in solid iron: implications for the composition of Earth's core. Earth Planet. Sci. Lett. 254, 233–238.

Bennett, N.R., Brenan, J.M., Fei, Y., 2016. Thermometry of the magma ocean: Controls on the metal–silicate partitioning of gold. Geochim. Cosmochim. Acta 184, 173–192.

Bermingham, K.R., Worsham, E.A., Walker, R.J., 2018. New insights into Mo and Ru isotope variation in the nebula and terrestrial planet accretionary genetics. Earth Planet. Sci. Lett. 487, 221–229.

Bouhifd, M.A., Jephcoat, A.P., 2011. Convergence of Ni and Co metal–silicate partition coefficients in the deep magma-ocean and coupled silicon–oxygen solubility in iron melts at high pressures. Earth Planet. Sci. Lett. 307, 341–348.

Boujibar, A., Andrault, D., Bouhifd, M.A., Bolfan-Casanova, N., Devidal, J.L., Trcera, N., 2014. Metal–silicate partitioning of sulphur, new experimental and thermodynamic constraints on planetary accretion. Earth Planet. Sci. Lett. 391, 42–54.

Boujibar, A., Habermann, M., Righter, K., Ross, D.K., Pando, K., Righter, M., Chidester, B. A., Danielson, L.R., 2019. U, Th, and K partitioning between metal, silicate, and sulfide and implications for Mercury's structure, volatile content, and radioactive heat production. Am. Mineral. 104, 1221–1237.

Boujibar, A., Righter, K., Bullock, E.S., Du, Z., Fei, Y., 2020. Segregation of Na, K, Rb and Cs into the cores of Earth, Mars and Vesta constrained with partitioning experiments. Geochim. Cosmochim. Acta 269, 622–638.

Brenan, J.M., McDonough, W.F., 2009. Core formation and metal–silicate fractionation of osmium and iridium from gold. Nat. Geosci. 2, 798–801.

Brenan, J.M., Mungall, J.E., Bennett, N.R., 2019. Abundance of highly siderophile elements in lunar basalts controlled by iron sulfide melt. Nat. Geosci. 12, 701–706.

Brennan, M.C., Fischer, R.A., Irving, J.C., 2020. Core formation and geophysical properties of Mars. Earth Planet. Sci. Lett. 530, 115923.

Budde, G., Burkhardt, C., Kleine, T., 2019. Molybdenum isotopic evidence for the late accretion of outer Solar System material to Earth. Nat. Astron. 3, 736–741.

Campbell, A.J., Humayun, M., Weisberg, M.W., 2002. Siderophile element constraints on the formation of metal in the metal-rich chondrites Bencubbin, Weatherford, and Gujba. Geochim. Cosmochim. Acta 66, 647–660.

Capobianco, C.J., Drake, M.J., de'Aro, J., 1999. Siderophile geochemistry of Ga, Ge, and Sn: cationic oxidation states in silicate melts and the effect of composition in iron–nickel alloys. Geochim. Cosmochim. Acta 63, 2667–2677.

Cartier, C., Hammouda, T., Boyet, M., Bouhifd, M.A., Devidal, J.-L., 2014. Redox control of the fractionation of niobium and tantalum during planetary accretion and core formation. Nat. Geosci. 7, 573–576.

Cartier, C., Namur, O., Nittler, L.R., Weider, S.Z., Crapster-Pregont, E., Vorburger, A., Frank, E.A., Charlier, B., 2020. No FeS layer in Mercury? Evidence from Ti/Al measured by MESSENGER. Earth Planet. Sci. Lett. 534, 116108.

Chabot, N.L., Draper, D.S., Agee, C.B., 2005. Conditions of core formation in the Earth: constraints from nickel and cobalt partitioning. Geochim. Cosmochim. Acta 69, 2141–2151.

Corgne, A., Keshav, S., Wood, B.J., McDonough, W.F., Fei, Y., 2008. Metal–silicate partitioning and constraints on core composition and oxygen fugacity during Earth accretion. Geochim. Cosmochim. Acta 72, 574–589.

Cottrell, E., Walker, D., 2006. Constraints on core formation from Pt partitioning in mafic silicate liquids at high temperatures. Geochim. Cosmochim. Acta 70, 1565–1580.

Creech, J.B., Baker, J.A., Handler, M.R., Lorand, J.-P., Storey, M., Wainwright, A.N., Luguet, A., Moynier, F., Bizzarro, M., 2017. Late accretion history of the terrestrial planets inferred from platinum stable isotopes. Geochem. Perspect. Lett. 3, 94–104.

Dauphas, N., 2017. The isotopic nature of the Earth's accreting material through time. Nature 541, 521–524.

Dauphas, N., Pourmand, A., 2011. Hf–W–Th evidence for rapid growth of Mars and its status as a planetary embryo. Nature 473, 489–492.

Dauphas, N., Davis, A.M., Marty, B., Reisberg, L., 2004. The cosmic molybdenum–ruthenium isotope correlation. Earth Planet. Sci. Lett. 226, 465–475.

Dauphas, N., Burkhardt, C., Warren, P.H., Fang-Zhen, T., 2014. Geochemical arguments for an Earth-like Moon-forming impactor. Phil. Trans. R. Soc. Lon. A 372, 20130244.

Day, J.M., O'Driscoll, B., 2019. Ancient high Pt/Os crustal contaminants can explain radiogenic ^{186}Os in some intraplate magmas. Earth Planet. Sci. Lett. 519, 101–108.

Day, J.M., Walker, R.J., Warren, J.M., 2017. ^{186}Os–^{187}Os and highly siderophile element abundance systematics of the mantle revealed by abyssal peridotites and Os-rich alloys. Geochim. Cosmochim. Acta 200, 232–254.

Debaille, V., Brandon, A.D., O'Neill, C., Yin, Q.Z., Jacobsen, B., 2009. Early martian mantle overturn inferred from isotopic composition of nakhlite meteorites. Nat. Geosci. 2, 548–552.

Deguen, R., Landeau, M., Olson, P., 2014. Turbulent metal–silicate mixing, fragmentation, and equilibration in magma oceans. Earth Planet. Sci. Lett. 391, 274–287.

Ertel, W., O'Neill, H.S.C., Sylvester, P.J., Dingwell, D.B., 1999. Solubilities of Pt and Rh in a haplobasaltic silicate melt at 1300 °C. Geochim. Cosmochim. Acta 63, 2439–2449.

Ertel, W., Dingwell, D.B., Sylvester, P.J., 2008. Siderophile elements in silicate melts—A review of the mechanically assisted equilibration technique and the nanonugget issue. Chem. Geol. 248, 119–139.

Fiquet, G., Auzende, A.L., Siebert, J., Corgne, A., Bureau, H., Ozawa, H., Garbarino, G., 2010. Melting of peridotite to 140 gigapascals. Science 329, 1516–1518.

Fischer, R.A., Nakajima, Y., Campbell, A.J., Frost, D.J., Harries, D., Langenhorst, F., Rubie, D.C., 2015. High pressure metal-silicate partitioning of Ni Co, V, Cr, Si, and O. Geochim. Cosmochim. Acta 167, 177–194.

Fischer-Gödde, M., Kleine, T., 2017. Ruthenium isotopic evidence for an inner Solar System origin of the late veneer. Nature 541, 525–528.

Fischer-Gödde, M., Elfers, B.M., Münker, C., Szilas, K., Maier, W.D., Messling, N., Morishita, T., Van Kranendonk, M., Smithies, H., 2020. Ruthenium isotope vestige of Earth's pre-late-veneer mantle preserved in Archaean rocks. Nature 579, 240–244.

Foley, C.N., Wadhwa, M., Borg, L.E., Janney, P.E., Hines, R., Grove, T.L., 2005. The early differentiation history of Mars from ^{182}W–^{142}Nd isotope systematics in the SNC meteorites. Geochim. Cosmochim. Acta 69, 4557–4571.

Gaboardi, M., Humayun, M., 2009. Elemental fractionation during LA-ICP-MS analysis of silicate glasses: Implications for matrix-independent standardization. J. Anal. At. Spectrom. 24, 1188–1197.

Georg, R.B., Halliday, A.N., Schauble, E.A., Reynolds, B.C., 2007. Silicon in the Earth's core. Nature 447, 1102–1106.

Greenwood, R.C., Barrat, J.A., Miller, M.F., Anand, M., Dauphas, N., Franchi, I.A., Sillard, P., Starkey, N.A., 2018. Oxygen isotopic evidence for accretion of Earth's water before a high-energy Moon-forming giant impact. Sci. Adv. 4, p.eaao5928.

Haba, M.K., Lai, Y.J., Wotzlaw, J.F., Yamaguchi, A., Lugaro, M., Schönbächler, M., 2021. Precise initial abundance of Niobium-92 in the Solar System and implications for p-process nucleosynthesis. Proc Nat. Acad. Sci. U.S.A 118 e2017750118.

Hauck, S.A., Margot, J.L., Solomon, S.C., Phillips, R.J., Johnson, C.L., Lemoine, F.G., Mazarico, E., McCoy, T.J., Padovan, S., Peale, S.J., Perry, M.E., 2013. The curious case of Mercury's internal structure. J. Geophys. Res.: Planets 118, 1204–1220.

Hirose, K., Labrosse, S., Hernlund, J., 2013. Composition and state of the core. Annu. Rev. Earth Planet. Sci. 41, 657–691.

Hirose, K., Wood, B., Vočadlo, L., 2021. Light elements in the Earth's core. Nat. Rev. Earth Environ. 2, 645–658.

Holzheid, A., Palme, H., 1996. The influence of FeO on the solubilities of cobalt and nickel in silicate melts. Geochim. Cosmochim. Acta 60, 1181–1193.

Holzheid, A., Palme, H., Chakraborty, S., 1997. The activities of NiO, CoO and FeO in silicate melts. Chem. Geol. 139, 21–38.

Holzheid, A., Sylvester, P., O'Neill, H.S.C., Rubie, D.C., Palme, H., 2000. Evidence for a late chondritic veneer in the Earth's mantle from high-pressure partitioning of palladium and platinum. Nature 406, 396–399.

Hopp, T., Fischer-Gödde, M., Kleine, T., 2018. Ruthenium isotope fractionation in protoplanetary cores. Geochim. Cosmochim. Acta 223, 75–89.

Hopp, T., Budde, G., Kleine, T., 2020. Heterogeneous accretion of Earth inferred from Mo-Ru isotope systematics. Earth Planet. Sci. Lett. 534, 116065.

Huang, D., Siebert, J., Badro, J., 2021. High pressure partitioning behavior of Mo and W and late sulfur delivery during Earth's core formation. Geochim. Cosmochim. Acta 310, 19–31.

Humayun, M., 2012. Chondrule cooling rates inferred from diffusive profiles in metal lumps from the Acfer 097 CR2 chondrite. Meteorit. Planet. Sci. 47, 1191–1208.

Humayun, M., Simon, S.B., Grossman, L., 2007. Tungsten and hafnium distribution in calcium–aluminum inclusions (CAIs) from Allende and Efremovka. Geochim. Cosmochim. Acta 71, 4609–4627.

Iizuka, T., Lai, Y.J., Akram, W., Amelin, Y., Schönbächler, M., 2016. The initial abundance and distribution of ^{92}Nb in the Solar System. Earth Planet. Sci. Lett. 439, 172–181.

Ireland, T.J., Walker, R.J., Brandon, A.D., 2011. ^{186}Os-^{187}Os systematics of Hawaiian picrites: New insights into Os isotopic variations in oceanic island basalts. Geochim. Cosmochim. Acta 75, 4456–4475.

Jana, D., Walker, D., 1997. The impact of carbon on element distribution during core formation. Geochim. Cosmochim. Acta 61, 2759–2763.

Jennings, E.S., Jacobson, S.A., Rubie, D.C., Nakajima, Y., Vogel, A.K., Rose-Weston, L.A., Frost, D.J., 2021. Metal–silicate partitioning of W and Mo and the role of carbon in controlling their abundances in the Bulk Silicate Earth. Geochim. Cosmochim. Acta 293, 40–69.

Jochum, K.P., Weis, U., Stoll, B., Kuzmin, D., Yang, Q., Raczek, I., Günther, D., 2011. Determination of reference values for NIST SRM 610–617 glasses following ISO guidelines. Geostand. Geoanal. Res. 35, 397–429.

Jones, J.H., Drake, M.J., 1986. Geochemical constraints on core formation in the Earth. Nature 322, 221–228.

Kendall, J., Melosh, H.J., 2016. Differentiated planetesimal impacts into a terrestrial magma ocean: fate of the iron core. Earth Planet. Sci. Lett. 448, 24–33.

Kruijer, T.S., Kleine, T., Borg, L.E., Brennecka, G.A., Irving, A.J., Bischoff, A., Agee, C.B., 2017. The early differentiation of Mars inferred from Hf–W chronometry. Earth Planet. Sci. Lett. 474, 345–354.

Labrosse, S., Hernlund, J.W., Coltice, N., 2007. A crystallizing dense magma ocean at the base of the Earth's mantle. Nature 450, 866–869.

Lapen, T.J., Righter, M., Brandon, A.D., Debaille, V., Beard, B.L., Shafer, J.T., Peslier, A. H., 2010. A younger age for ALH84001 and its geochemical link to shergottite sources in Mars. Science 328, 347–351.

Lapen, T.J., Righter, M., Andreasen, R., Irving, A.J., Satkoski, A.M., Beard, B.L., 2017. Two billion years of magmatism recorded from a single Mars meteorite ejection site. Sci. Adv. 3 (2).

Laurenz, V., Rubie, D.C., Frost, D.J., Vogel, A.K., 2016. The importance of sulfur for the behaviour of highly-siderophile elements during Earth's differentiation. Geochim. Cosmochim. Acta 194, 123–138.

Lee, D.C., Halliday, A.N., 1997. Core formation on Mars and differentiated asteroids. Nature 388, 854–857.

Lewis, R.D., Lofgren, G.E., Franzen, H.F., Windom, K.E., 1993. The effect of Na vapor on the Na content of chondrules. Meteoritics 28, 622–628.

Lherm, V., Deguen, R., 2018. Small-Scale metal/silicate equilibration during core formation: The influence of stretching enhanced diffusion on mixing. J. Geophys. Res.: Solid Earth 123, 10–496.

Li, Y., Dasgupta, R., Tsuno, K., 2015. The effects of sulfur, silicon, water, and oxygen fugacity on carbon solubility and partitioning in Fe-rich alloy and silicate melt systems at 3 GPa and 1600 C: Implications for core–mantle differentiation and degassing of magma oceans and reduced planetary mantles. Earth Planet. Sci. Lett. 415, 54–66.

Lin, J.F., Struzhkin, V.V., Sturhahn, W., Huang, E., Zhao, J.Y., Hu, M.Y., Alp, E.E., Mao, H.K., Boctor, N., Hemley, R.J., 2003. Sound velocities of iron–nickel and iron–silicon alloys at high pressures. Geophys. Res. Lett. 30, no. 21.

Lupis, C. H., 1983. Chemical thermodynamics of materials. Elsevier Science Publishing Co., Inc., 581 pp.

Ma, Z., 2001. Thermodynamic description for concentrated metallic solutions using interaction parameters. Metall. Mat. Trans. B 32, 87–103.

MacKenzie, J.M., Canil, D., 2008. Volatile heavy metal mobility in silicate liquids: Implications for volcanic degassing and eruption prediction. Earth Planet. Sci. Lett. 269, 488–496.

Malavergne, V., Cordier, P., Righter, K., Brunet, F., Zanda, B., Addad, A., Smith, T., Bureau, H., Surblé, S., Raepsaet, C., Charon, E., 2014. How Mercury can be the most reduced terrestrial planet and still store iron in its mantle. Earth Planet. Sci. Lett. 394, 186–197.

Malavergne, V., Charon, E., Jones, J., Cordier, P., Righter, K., Deldicque, D., Hennet, L., 2016. The formation of nuggets of highly siderophile elements in quenched silicate melts at high temperatures: Before or during the silicate quench? Earth Planet. Sci. Lett. 434, 197–207.

Mann, U., Frost, D.J., Rubie, D.C., Becker, H., Audétat, A., 2012. Partitioning of Ru, Rh, Pd, Re, Ir and Pt between liquid metal and silicate at high pressures and high temperatures-Implications for the origin of highly siderophile element concentrations in the Earth's mantle. Geochim. Cosmochim. Acta 84, 593–613.

Mao, Z., Lin, J.-F., Liu, J., Alatas, A., Gao, L., Zhao, J., Mao, H.-K., 2012. Sound velocities of Fe and Fe-Si alloy in the Earth's core. Proc. Nat. Acad. Sci. U.S.A. 109, 10239–10244.

Médard, E., Schmidt, M.W., Wälle, M., Keller, N.S., Günther, D., 2015. Platinum partitioning between metal and silicate melts: Core formation, late veneer and the nanonuggets issue. Geochim. Cosmochim. Acta 162, 183–201.

Mundl-Petermeier, A., Walker, R.J., Fischer, R.A., Lekic, V., Jackson, M.G., Kurz, M.D., 2020. Anomalous ^{182}W in high ^{3}He/^{4}He oceanic island basalts: Fingerprints of Earth's core? Geochim. Cosmochim. Acta 271, 194–211.

Münker, C., Fonseca, R.O.C., Schulz, T., 2017. Silicate Earth's missing niobium may have been sequestered into asteroidal cores. Nat, Geosci. 10, 822–826.

Namur, O., Charlier, B., Holtz, F., Cartier, C., McCammon, C., 2016. Sulfur solubility in reduced mafic silicate melts: Implications for the speciation and distribution of sulfur on Mercury. Earth Planet. Sci. Lett. 448, 102–114.

Newsom, H.E., Drake, M.J., 1983. Experimental investigation of the partitioning of phosphorus between metal and silicate phases: Implications for the Earth, Moon and eucrite parent body. Geochim. Cosmochim. Acta 47, 93–100.

Nimmo, F., Kleine, T., 2007. How rapidly did Mars accrete? Uncertainties in the Hf–W timing of core formation. Icarus 191, 497–504.

O'Neill, H.S.C., Dingwell, D.B., Borisov, A., Spettel, B., Palme, H., 1995. Experimental petrochemistry of some highly siderophile elements at high temperatures, and some implications for core formation and the mantle's early history. Chem. Geol. 120, 255–273.

Palme, H., O'Neill, H.S.C., 2014. Cosmochemical estimates of mantle composition. Treatise on Geochemistry 2. 2nd ed. Pp. 1–39.

Righter, K., 2011. Prediction of metal–silicate partition coefficients for siderophile elements: an update and assessment of PT conditions for metal–silicate equilibrium during accretion of the Earth. Earth Planet. Sci. Lett. 304, 158–167.

Righter, K., 2015. Modeling siderophile elements during core formation and accretion, and the role of the deep mantle and volatiles. Am. Mineral. 100, 1098–1109.

Righter, K., 2016. Metal-silicate partitioning of siderophile elements and core-mantle segregation. *Deep Earth: Physics and Chemistry of the Lower Mantle and Core*, AGU Geophys. Monogr. Series 161–179.

Righter, K., Shearer, C.K., 2003. Magmatic fractionation of Hf and W: constraints on the timing of core formation and differentiation in the Moon and Mars. Geochim. Cosmochim. Acta 67, 2497–2507.

Righter, K., Drake, M.J., Yaxley, G., 1997. Prediction of siderophile element metal-silicate partition coefficients to 20 GPa and 2800 C: the effects of pressure, temperature, oxygen fugacity, and silicate and metallic melt compositions. Phys. Earth Planet. Inter. 100, 115–134.

Righter, K., Humayun, M., Danielson, L.R., 2008. High pressure and temperature partitioning of palladium during core formation. Nat. Geosci. 1, 321–323.

Righter, K., Pando, K., Danielson, L.R., Lee, C.-T., 2010. Partitioning of Mo, P and other siderophile elements (Cu, Ga, Sn, Ni Co, Cr, Mn, V, W) between metal and silicate melt as a function of temperature and melt composition. Earth Planet. Sci. Lett. 291, 1–9.

Righter, K., King, C., Danielson, L.R., Pando, K., Lee, C.-T., 2011. Experimental determination of the metal/silicate partition coefficient of Germanium: Implications for core and mantle differentiation. Earth Planet. Sci. Lett. 304, 379–388.

Righter, K., Danielson, L.R., Pando, K., Williams, J., Humayun, M., Hervig, R.L., Sharp, T. G., 2015. Mantle HSE abundances in Mars due to core formation at high pressure and temperature. Meteorit. Planet. Sci. 50, 604–631.

Righter, K., Danielson, L.R., Pando, K.M., Shofner, G.A., Sutton, S.R., Newville, M., Lee, C.T., 2016. Valence and metal/silicate partitioning of Mo: Implications for conditions of Earth accretion and core formation. Earth Planet. Sci. Lett. 437, 89–100.

Righter, K., Nickodem, K., Pando, K., Danielson, L., Boujibar, A., Righter, M., Lapen, T.J., 2017. Distribution of Sb, As, Ge, and In between metal and silicate during accretion and core formation in the Earth. Geochim. Cosmochim. Acta 198, 1–16.

Righter, K., Pando, K., Humayun, M., Waeselmann, N., Yang, S., Boujibar, A., Danielson, L.R., 2018. Effect of silicon on activity coefficients of siderophile elements (Au, Pd, Pt, P, Ga, Cu, Zn, and Pb) in liquid Fe: Roles of core formation, late sulfide matte, and late veneer in shaping terrestrial mantle geochemistry. Geochim. Cosmochim. Acta 232, 101–123.

Righter, K., Pando, K., Ross, D.K., Righter, M., Lapen, T.J., 2019. Effect of silicon on activity coefficients of Bi, Cd, Sn, and Ag in liquid Fe-Si, and implications for differentiation and core formation. Meteorit. Planet. Sci. 54, 1379–1394.

Righter, K., Schönbächler, M., Pando, K., Rowland II, R., Righter, M., Lapen, T., 2020. Ag isotopic and chalcophile element evolution of the terrestrial and martian mantles during accretion: New constraints from Bi and Ag metal-silicate partitioning. Earth Planet. Sci. Lett. 552, 116590.

Rizo, H., Andrault, D., Bennett, N.R., Humayun, M., Brandon, A., Vlastélic, I., Murphy, D. T., 2019. ^{182}W evidence for core-mantle interaction in the source of mantle plumes. Geochem. Perspect. Lett. 11, 6–11.

Rubie, D.C., Laurenz, V., Jacobson, S.A., Morbidelli, A., Palme, H., Vogel, A.K., Frost, D. J., 2016. Highly siderophile elements were stripped from Earth's mantle by iron sulfide segregation. Science 353, 1141–1144.

Sanloup, C., Fiquet, G., Gregoryanz, E., Morard, G., Mezouar, M., 2004. Effect of Si on liquid Fe compressibility: Implications for sound velocity in core materials. Geophys. Res. Lett. 31 (7).

Siebert, J., Corgne, A., Ryerson, F.J., 2011. Systematics of metal–silicate partitioning for many siderophile elements applied to Earth's core formation. Geochim. Cosmochim. Acta 75, 1451–1489.

Siebert, J., Badro, J., Antonangeli, D., Ryerson, F.J., 2013. Terrestrial accretion under oxidizing conditions. Science 339, 1194–1197.

Smith, D.E., Zuber, M.T., Phillips, R.J., Solomon, S.C., Hauck, S.A., Lemoine, F.G., Mazarico, E., Neumann, G.A., Peale, S.J., Margot, J.L., Johnson, C.L., 2012. Gravity field and internal structure of Mercury from MESSENGER. Science 336, 214–217.

Steelmaking, J., 1988. Steelmaking Data Sourcebook. Gordon and Breach Science Publishers, Montreux.

Steenstra, E.S., Seegers, A.X., Putter, R., Berndt, J., Klemme, S., Matveev, S., Bullock, E. S., van Westrenen, W., 2020. Metal-silicate partitioning systematics of siderophile elements at reducing conditions: A new experimental database. Icarus 335, 113391.

Steenstra, E.S., Berndt, J., Rohrbach, A., Bullock, E.S., van Westrenen, W., Klemme, S., Walter, M.J., 2022. Partitioning of Ru, Pd, Ag, Re, Pt, Ir and Au between sulfide-, metal-and silicate liquid at highly reduced conditions: Implications for terrestrial accretion and aubrite parent body evolution. Geochim. Cosmochim. Acta 336, 15–32.

Suer, T.A., Siebert, J., Remusat, L., Day, J., Borensztajn, S., Doisneau, B., Fiquet, G., 2021. Reconciling metal–silicate partitioning and late accretion in the Earth. Nat. Comm. 12, 1–10.

Szumila, I., Trail, D., Danielson, L.R., 2019. The effect of fO_2 on the diffusion of redox-sensitive elements in haplobasaltic melt at 1 GPa and 1300° C. Chem. Geol. 512, 107–120.

Tang, H., Dauphas, N., 2014. ^{60}Fe–^{60}Ni chronology of core formation in Mars. Earth Planet. Sci. Lett. 390, 264–274.

Taylor, G.J., 2013. The bulk composition of Mars. Geochemistry 73, 401–420.

Touboul, M., Puchtel, I.S., Walker, R.J., 2012. ^{182}W evidence for long-term preservation of early mantle differentiation products. Science 335, 1065–1069.

Tsuno, K., Frost, D.J., Rubie, D.C., 2013. Simultaneous partitioning of silicon and oxygen into the Earth's core during early Earth differentiation. Geophys. Res. Lett. 40, 66–71.

Tuff, J., Wood, B.J., Wade, J., 2011. The effect of Si on metal-silicate partitioning of siderophile elements and implications for the conditions of core formation Geochim. Cosmochim. Acta 75, 673–690.

Vogel, A.K., Jennings, E.S., Laurenz, V., Rubie, D.C., Frost, D.J., 2018. The dependence of metal-silicate partitioning of moderately volatile elements on oxygen fugacity and Si contents of Fe metal: Implications for their valence states in silicate liquids. Geochim. Cosmochim. Acta 237, 275–293.

Wade, J., Wood, B.J., 2001. The Earths missing niobium may be in the core. Nature 409, 75–78.

Wade, J., Wood, B.J., 2005. Core formation and the oxidation state of the Earth. Earth Planet. Sci. Lett. 236, 78–95.

Wade, J., Wood, B.J., Tuff, J., 2012. Metal–silicate partitioning of Mo and W at high pressures and temperatures: evidence for late accretion of sulphur to the Earth. Geochim. Cosmochim. Acta 85, 58–74.

Walker, R.J., 2009. Highly siderophile elements in the Earth, Moon and Mars: update and implications for planetary accretion and differentiation. Geochemistry 69, 101–125.

Walker, R.J., McDonough, W.F., Honesto, J., Chabot, N.L., McCoy, T.J., Ash, R.D., Bellucci, J.J., 2008. Modeling fractional crystallization of group IVB iron meteorites. Geochim. Cosmochim. Acta 72, 2198–2216.

Wang, L., Fei, Y., 2023. A partially equilibrated initial mantle and core indicated by stress-induced percolative core formation through a bridgmanite matrix. Sci. Adv. 9, eade3010.

Wang, J., Xiong, X., Takahashi, E., Zhang, L., Li, L., Liu, X., 2019. Oxidation state of arc mantle revealed by partitioning of V, Sc, and Ti between mantle minerals and basaltic melts. J. Geophys. Res.: Solid Earth 124, 4617–4638.

Warren, P.H., 2011. Stable-isotopic anomalies and the accretionary assemblage of the Earth and Mars: A subordinate role for carbonaceous chondrites. Earth Planet. Sci. Lett. 311, 93–100.

Wasson, J.T., Ouyang, X., Wang, J., Jerde, E., 1989. Chemical classification of iron meteorites: XI. Multi-element studies of 38 new irons and the high abundance of ungrouped irons from Antarctica. Geochim. Cosmochim. Acta 53, 735–744.

Wood, B.J., 2008. Accretion and core formation: constraints from metal–silicate partitioning. Phi.l Trans. R. Soc. London Ser. A 366, 4339–4355.

Wood, B.J., Walter, M.J., Wade, J., 2006. Accretion of the Earth and segregation of its core. Nature 441, 825–833.

Wood, B.J., Kiseeva, E.S., Mirolo, F.J., 2014. Accretion and core formation: The effects of sulfur on metal–silicate partition coefficients. Geochim. Cosmochim. Acta 145, 248–267.

Worsham, E.A., Burkhardt, C., Budde, G., Fischer-Gödde, M., Kruijer, T.S., Kleine, T., 2019. Distinct evolution of the carbonaceous and non-carbonaceous reservoirs: Insights from Ru, Mo, and W isotopes. Earth Planet. Sci. Lett. 521, 103–112.

Yang, S., Humayun, M., Righter, K., Jefferson, G., Fields, D., Irving, A.J., 2015. Siderophile and chalcophile element abundances in shergottites: Implications for Martian core formation. Meteorit. Planet. Sci. 50, 691–714.

Yang, S., Humayun, M., Salters, V.J.M., 2018. Elemental systematics in MORB glasses from the Mid-Atlantic Ridge. Geochem. Geophys. Geosys. 19, 4236–4259.

Yokoyama, T., Walker, D., Walker, R.J., 2009. Low osmium solubility in silicate at high pressures and temperatures. Earth Planet. Sci. Lett. 279, 165–173.

Zhang, Y., Ni, H., Chen, Y., 2010. Diffusion data in silicate melts. Rev. Mineral. Geochem. 72, 311–408.

Ziegler, K., Young, E.D., Schauble, E.A., Wasson, J.T., 2010. Metal–silicate silicon isotope fractionation in enstatite meteorites and constraints on Earth's core formation. Earth Planet. Sci. Lett. 295, 487–496.